Coupling active and passive techniques to control the flow past the square back Ahmed body

Charles-Henri Bruneau [a,*], Emmanuel Creusé [b], Delphine Depeyras [a], Patrick Gilliéron [c], Iraj Mortazavi [a]

[a] IMB, Université Bordeaux 1, Team MC2 INRIA Bordeaux-Sud-Ouest, UMR 5251 CNRS, France
[b] Team SIMPAF INRIA Lille Nord Europe, Laboratoire Paul Painlevé, UMR 8524 CNRS, Université Lille 1, Sciences et Technologies, Cité Scientifique, F-59655 Villeneuve d'Ascq, France
[c] Technocentre Renault, Direction de La Recherche, Mécanique des fluides et aérodynamique DREAM/DTAA, Code API: TCR AVA 058 1, Avenue du Golf, F-78288 Guyancourt, France

ABSTRACT

Several active and passive control techniques are used to reduce the drag coefficient of the square back Ahmed body. The results are carefully analyzed and compared to each other. The final goal of this paper is to show that it is possible to couple passive and active control techniques to improve the flow control. In the present study, a drag reduction of 30% is achieved, almost corresponding to the goal of automotive industry.

© 2010 Elsevier Ltd. All rights reserved.

1. Introduction

The research developed today in car aerodynamics is carried out from the point of view of the durable development. Some car companies have the objective to develop control solutions able to reduce at least 30% of the aerodynamic drag of the vehicles without constraints on the design, the comfort, the storage or the safety of the passengers. Thus, it is necessary to modify locally the flow, to remove or delay the separation position or to reduce the development of the recirculation zone at the back and of the separated swirling structures [15]. This can be mainly obtained by controlling the flow near the wall with or without additional energy using active or passive devices [14,15]. Significant results can be obtained using simple techniques [29,5]. In practise, the flow control is obtained when the wall pressure distribution is successfully modified on the back and on the rear window, using various adapted devices which change locally the geometry. Control experiments in wind tunnel on reduced or real ground vehicles are performed and measurements of the wall static pressures and of the aerodynamic torque allow to quantify the effect of the control [17,12,15,29,30]. However, due to the design constraints, the real gain is rather weak and so new control techniques have to be developed. Among these new techniques in progress, separate devices located in front of or behind the vehicle can be used to reduce the development of the recirculation zone on the rear window or at the back and the interactions of the swirling wake structures.

A famous benchmark that is commonly used in the ground vehicle industry is the Ahmed body [2]. It is a three-dimensional bluff body moving in the vicinity of the ground generating a turbulent flow. Several separations appear along the body from the front to the back [26]. The resulting recirculation zones contribute to a significant part of the drag coefficient [18,19,27]. This coefficient changes strongly with the angle α between the horizontal line and the rear window (for both the 2D and 3D flows, a minimum is achieved around $\alpha = 12°$ and a maximum around $\alpha = 30°$). For a square back Ahmed body (without a rear window), the flow separates at the back and is mainly a two-dimensional base flow. Indeed, experimental and numerical studies confirm the two-dimensional behaviour of the detached near-wall flow at the base of the square back Ahmed body geometry [30,17,23,8,20]. On the contrary, for the angles α situated in the range of 12–30°, the flow is highly three-dimensional over the rear window as there are two counter-rotating lateral vortices and an open separation zone [27,17,30,24,20]. In this paper we focus on the square back Ahmed body ($\alpha = 0°$) corresponding to simplified mono space cars or trucks and thus two-dimensional results are mainly presented. The main objective is then to reduce the separated area at the back and thus the static and total pressure gradients that govern the aerodynamic drag. Two-dimensional computations cannot give the exact values of the drag around the three-dimensional Ahmed body but allows to understand the trends of the control with respect to the uncontrolled case. Moreover, the computational domain is restricted to a short area around the body as in any cases the wake flow is strongly three-dimensional.

In order to control the flow around the square back Ahmed body, Rouméas et al. [30] implemented four blowing slots around the three-dimensional rear end of the body. The angle between

* Corresponding author.
E-mail addresses: bruneau@math.u-bordeaux1.fr (C.-H. Bruneau), creuse@math.univ-lille1.fr (E. Creusé), depeyras@math.u-bordeaux1.fr (D. Depeyras), patrick.gillieron@renault.com (P. Gilliéron), mortaz@math.u-bordeaux1.fr (I. Mortazavi).

every uniform jet and the wall was $\theta = 45°$ inward, reducing the near wake spanwise cross-section. For an optimal blowing velocity of half the amplitude of the mean flow, the drag forces were decreased up to 20%. In [8], Brunn et al. studied an Ahmed configuration quite close to the bus-shape Ahmed body that corresponds to a $\alpha = 35°$ rear window slant angle. The flow was then controlled, reducing the separation bubble on the slant, thanks to a periodic excitation using a synthetic jet along the upper window section with the roof. The control was tuned for a wide range of Strouhal numbers (based on the inflow velocity and the car model height $0.1 \leqslant St \leqslant 0.9$) and a forcing intensity (based on the inflow velocity, the jet velocity, the height of the body and the thickness of the actuator) of $C_\mu = 4 \times 10^{-3}$. They achieved a drastic reduction of the recirculation area in the close wake and converged towards the formation of two longitudinal structures at the slant corners. Both structures formation procedure has a direct effect on the efficiency of the control.

In a recent work Bruneau et al. [6] introduced a passive control technique using a porous slice implemented on some parts of the two-dimensional square back Ahmed body in a free domain or on top of a road, reducing global quantities such as the drag coefficient, the enstrophy or the C_{Lrms} of the flow. This new passive approach seems very promising as significant gains were obtained with a good choice of the layers location. The presence of a road decreases the efficiency of the control but does not alter the general tendency observed without the road.

In this paper, a new strategy that corresponds to coupling both passive and active control approaches is performed on the square-back Ahmed body on top of a road. The main goal is to explore how efficiently it is possible to couple active and passive control procedures that are separately beneficial or not in order to reduce the aerodynamic drag forces.

The paper is organised as follows: after a quick overview of the modelling approach and the numerical simulation techniques, the physical dynamics of the flow and its pseudo two-dimensional behaviour is analysed. Then, some active control methods using steady jets, pulsed jets and closed-loop jets as well as the passive control using porous layers, are implemented to this geometry and their effects on the drag reduction process are studied. The last part of the paper is devoted to a detailed analysis of the coupling control scenarios between active and passive techniques. It is shown how far it's possible to introduce such strategies in order to increase the efficiency of the control of the flow with the smallest possible energetic consumption.

2. Modelling and numerical simulation

In this section, the method used to simulate the flow past Ahmed body on top of a road using Cartesian grids is presented. To compute the flow around solid bodies an immersed boundary model is used, namely the penalised Navier–Stokes equations for the velocity and pressure (U,p) as unknowns ([1,5]) that read on the non dimensional form based on the density ρ, the velocity at the entrance section U_∞ and the heigth H of the Ahmed body

$$\partial_t U + (U \cdot \nabla)U - \frac{1}{Re}\Delta U + \frac{U}{K} + \nabla p = 0 \ in \ \Omega_T = \Omega \times (0,T) \tag{1}$$

$$\nabla \cdot U = 0 \ in \ \Omega_T \tag{2}$$

where Re is the non dimensional Reynolds number based on the length L of the body as usually done in the car industry, K is the non dimensional coefficient of permeability of the medium and Ω is the full domain including the porous layer and the solid body. In the fluid the permeability coefficient goes to infinity, the penalisation term vanishes and we solve the non dimensional Navier–Stokes equations. In the solid body the permeability coefficient goes to zero and it has been shown in [1] that solving these equations corre-

sponds to solve Darcy's law in the solid and that the velocity is proportional to K. For numerical simulations we set $K = 10^{16}$ in the fluid and $K = 10^{-8}$ in the solid body. Let us note that with the L^2-penalization above there is no numerical boundary layer at order zero contrarily to the H^1-penalization [1]. There is a numerical boundary layer at order one and if the normal derivative is required at the interface it is possible to improve the method as shown in [11]. The only drawback is the fact that the body has not exactly the real size as it does not fit the mesh. Finally with the small value $K = 10^{-8}$, the velocity inside the body is of the same order and the interface body-fluid is really a solid-fluid interface. For values bigger than 10^{-5}, the body resembles a porous medium and the interface changes as we shall see below.

The Eqs. (1) and (2) above are associated to an initial datum $(X = (x,y,z))$:

$$U(X,0) = U_0(X) \ in \ \Omega$$

and the following boundary conditions:

$U = U_\infty = (u_\infty,0,0) = (1,0,0)$ on the entrance section and on the road;

$\sigma(U,p)n + \frac{1}{2}(U \cdot n)^-(U - U_{ref}) = \sigma(U_{ref},p_{ref})n$ on the open boundaries to convey properly the vortices through the artificial frontiers [3], where $\sigma(U,p) = 1/Re(\nabla U + \nabla U^t) - p\,I$ is the stress tensor, n is the unit normal pointing outside of the domain and for a real number a the notation $a = a^+ - a^-$ is used.

Then a numerical simulation is performed solving directly the Navier–Stokes equations and using a second-order Gear scheme in time with explicit treatment of the convection term. All the linear terms are treated implicitly and discretized via a second-order centered finite differences scheme. The CFL condition related to the convection term requires a time step of the order of magnitude of the space step as U is of order one. A third-order finite differences upwind scheme is used for the space discretization of the convection terms. This scheme has been tested extensively on the lid-driven cavity problem and is proven to be stable and accurate with very few diffusive effects as it compares very well with spectral methods [7]. The efficiency of the resolution is obtained by a multigrid procedure using a cell-by-cell relaxation smoother.

All the simulations are performed on the domain $\Omega = (0,15) \times (0,5)$ in two dimensions (see the Fig. 2) with a 1920×640 cells uniform mesh and $\Omega = (0,12) \times (0,6) \times (0,4)$ in three dimensions with a $768 \times 384 \times 256$ cells uniform mesh. The grid convergence for the same geometry has been studied in [6] and the grid 960×320 corresponds already to the finest grid required. The velocity vector is $U = (u,w)$ in two dimensions and $U = (u,v,w)$ in three-dimensions. The Reynolds number based on the length $L = 3.625H$ of the body is 30,000 that corresponds to $Re = 8,275$. The spanwise dimension is $l = 1.35H$. The choice of this medium Reynolds number ensures the grid convergence in 2D on a reasonable grid size that is almost reachable in 3D. Moreover, the laboratory experiments are often restricted to the same range of Reynolds numbers [28].

For the active control, we add an horizontal jet $U_j = (u_j,0,0)$ at the back of the body as shown in the Fig. 1. The horizontal jet has a non dimensional thickness $h_j = 0.024$ and an amplitude A ($u_j = A\,u_\infty$) which corresponds to the forcing intensity $C_\mu = \frac{h_j}{H}\left(\frac{u_j}{u_\infty}\right)^2$. To represent this jet, the velocity is given on the back in the last solid cell, the next cell being in the fluid. As the jet is coming out of the body, taken into account by the penalization method, the divergence-free condition (2) is locally modified as

$$\nabla \cdot U = \frac{u_j}{\delta x} \tag{3}$$

with δx the horizontal space step in order to avoid the flow come back into the body. This modification is coupled to the penalization method in the solid and does affect neither the mass conservation on the other cells nor the flow computation.
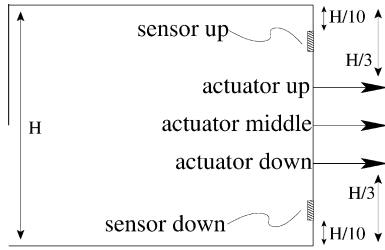
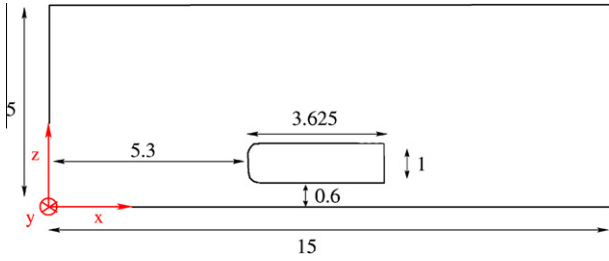Fig. 1. Actuators and sensors locations for the active control at the back of Ahmed body.

Fig. 2. Computational domain around the square back Ahmed body.

For the passive control, porous layers of thickness $h = 0.1\,H$ are inserted on some parts of the Ahmed body [4]. Using the above mentioned meshes, a significant number of points are included in the porous layer. With the penalization method, solving the flow inside a porous medium of high porosity is reduced to set an intermediate value of K in the range 10^{-3} to 1 at the velocity points inside the porous layers. Previous works have shown that a good value for the control is $K = 10^{-1}$ [4] related to a high intrinsic permeability medium. The addition of such layers is equivalent to solve the Navier–Stokes equations in the fluid with a Fourier-like boundary condition instead of the no-slip boundary condition [10]. Thus the shear effects in the boundary layer are reduced. Moreover a low speed laminar flow is created inside the layer. The conjunction of these two phenomena decreases significantly the drag force.

3. Flow characteristics and correlation with drag

3.1. Two-dimensional behaviour of the configuration

As mentioned in the introduction, the flow around the Ahmed body has a two or three-dimensional behaviour according to the angle of the rear window. However, for a square back body, the flow separates at the back and is similar to a two-dimensional base flow, dominated by counter-rotating structures. Experimental and numerical studies confirm the two-dimensional behaviour of the detached near-wall flow [2,30,17,16,23,8]. Here, a two-dimensional behaviour means that the flow is fully detached at the back without longitudinal structures, oppositely to what happens for the $\alpha = 25°$ rear window case. These characteristics are verified, computing the flow around the three-dimensional square back Ahmed body on top of a road at $Re = 30,000$. This computation has been performed on several consecutive grids and is validated by the results of the literature ([30] for the square-back and [20] for a rear window at $\alpha = 35°$). It is well-known that in both cases the behaviour of the base flow is almost two-dimensional and we find a very good agreement with other numerical results obtained with a URANS model, in particular for the streamlines on the mid plane. Moreover, although our computation is performed at a Reynolds number much lower than for real cars, the drag coef-
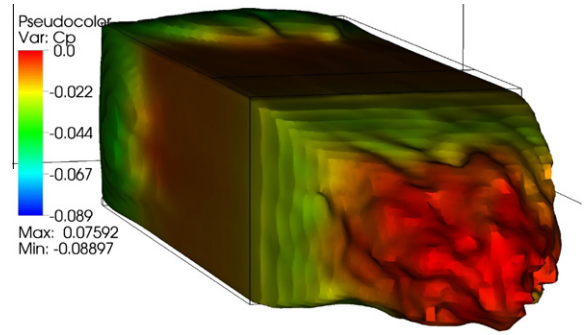

Fig. 3. C_{pi} = 0.9 isosurface colored with the C_p values of the three-dimensional mean flow around the square back Ahmed body at Reynolds number 30,000. (For interpretation of the references to colour in this figure legend, the reader is referred to the web version of this article.)

ficient $C_d = 0.315$ is comparable to the values available in the litterature around 0.26. So the numerical results are qualitatively and quantitatively relevant on the fine grid used. In Fig. 3 the C_p values on a constant isosurface of the total pressure loss coefficient C_{pi} are plotted. As the figure shows, the global behaviour of the isovalues corresponds to an almost uniform toric shape from the sides of the back very similar to the results in [30]. This is confirmed by the two-dimensional vertical cuts at $0.25\,l$ and $0.5\,l$ of the body that are compared to the two-dimensional simulation performed using the same mesh size (Fig. 4). Although they are more elongated, the mean vortices at the back are similar to the one obtained by the two-dimensional simulation. We observe in addition a decreasing evolution until the edge of the body $(0\,l)$, where no three-dimensional longitudinal vortex is generated as it is the case with a rear window at $\alpha = 25°$. Therefore, as a first simplified approach, the control strategies will be implemented on the two-dimensional configuration in this paper on a finer 1920×640 grid.

3.2. Properties of the flow

As the flow is computed inside the solid body with the penalisation method, we can compute the forces by integrating the penalisation term U/K on the volume of the body neglecting the time term and the convection term (see [9] for more details)

$$F_d = \int_{\partial body} \sigma(U,p)n\ d\gamma = \int_{body} \nabla \cdot \sigma(U,p)dX \approx \int_{body} \frac{U}{K}\ dX$$

where the body includes eventually the porous layers. Consequently the drag force $F_d \approx \int_{body} \frac{u}{K}\ dX$. This computation has been compared to the usual formula and a difference around 1% has been observed, therefore the above formula that is easier to compute is used all along the paper. To quantify the effect of the control we shall compare the static pressure coefficient C_p, the total pressure coefficient C_{p_i} and the drag coefficient C_d

$$C_p = 2(p - p_0)/|U|^2; \quad C_{p_i} = 2(p_i - p_{i0})/|U|^2;$$
$$C_d = \frac{F_d}{0.5\rho|U_\infty|^2 H} = \frac{2F_d}{H}$$

where $p_i = p + 1/2|U|^2$ is the total static pressure and the subscript 0 stands for the inlet quantities. Let us note that the mean value of the static pressure is set to zero at the downstream section of the computational domain.

The two-dimensional results are presented on a 1920×640 cells uniform mesh corresponding to
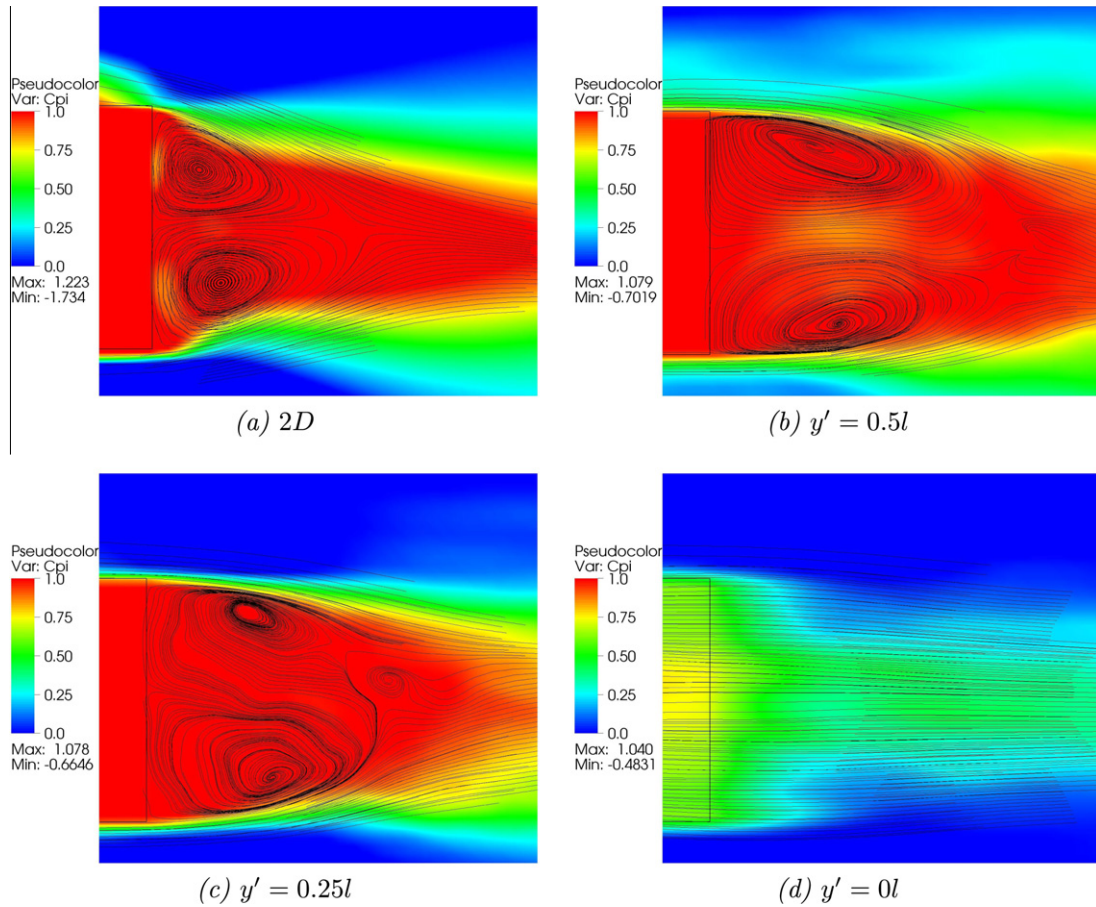
$$y^+ = \bar{y}\frac{u^+}{\nu} \approx 4 \tag{4}$$

Fig. 4. Streamlines and C_{pi} values for the two-dimensional mean flow (a) and three different spanwise sections y' of the three-dimensional mean flow (b–d).
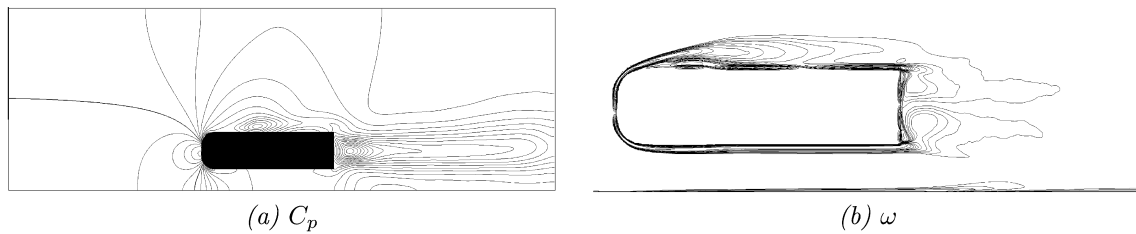

Fig. 5. Mean C_p and vorticity fields for the two-dimensional flow.

where $\bar{y}, u^+ = u_\infty \sqrt{0.0592/2Re^{0.2}}$ and v are respectively, the size of the first cell on the wall, the skin friction velocity and the kinematic viscosity of the fluid. The definition of the skin friction velocity by the Blasius power law corresponds to the laminar flow in the viscous sublayer. In these computations the space step is then $\delta x = \delta z = 1/128 = 0.0078125$ and the related time step $\delta t = 0.002$. The integration time over which the numerical simulations are performed is at least $T = 200$ and the statistics are gathered when the permanent regime is well established over about 3 shedding periods. The mean flows are obtained over at least 50,000 snapshots recorded every time step. The C_p isolines (tabulated everywhere from −3.4 to 3.4 by step 0.2) in Fig. 5 show a deep pressure well just behind the back wall corresponding to the vortex shedding as indicated by the vorticity field. The vorticity contours plotted are ±0.5, ±1, ±1.5, ±2, ±3, ±4, ±5, ±6, ±7, ±10, and ±15 all along the paper and the closest to zero are a little bit jagged. The contours reveal the presence of two strong vortices very close to the back which center is located between the corner and the middle of the back wall. To

control the flow, an efficient way is to vanish or to push away one or both such vortices. The position of the actuators is chosen to be located in front of these mean vortices.

3.3. Correlation between the instantaneous flow and the drag coefficient C_d

To complete this study we have chosen two monitoring points in the vicinity of the lower and the upper corners of the back to detect their individual frequencies. The dominant frequency $f = 0.25$ (Fig. 6) for two points near the corners corresponds to the mechanism of eddy formation and vortex shedding. These two points are located in the shedding layers that create the two counter-rotating vortices at the back. Using the corresponding eddy size and the averaged velocity, a Strouhal number $St = \frac{f\mathscr{L}}{\mathscr{V}}$ (based on the mean recirculation height $\mathscr{L}$ and on the mean velocity at the point $(9.0, 1.6)$ $\mathscr{V}$) of value $St = 0.22$ is found. This value agrees with the Strouhal number observed in other

(a) Upper corner $(9.0, 1.6)$
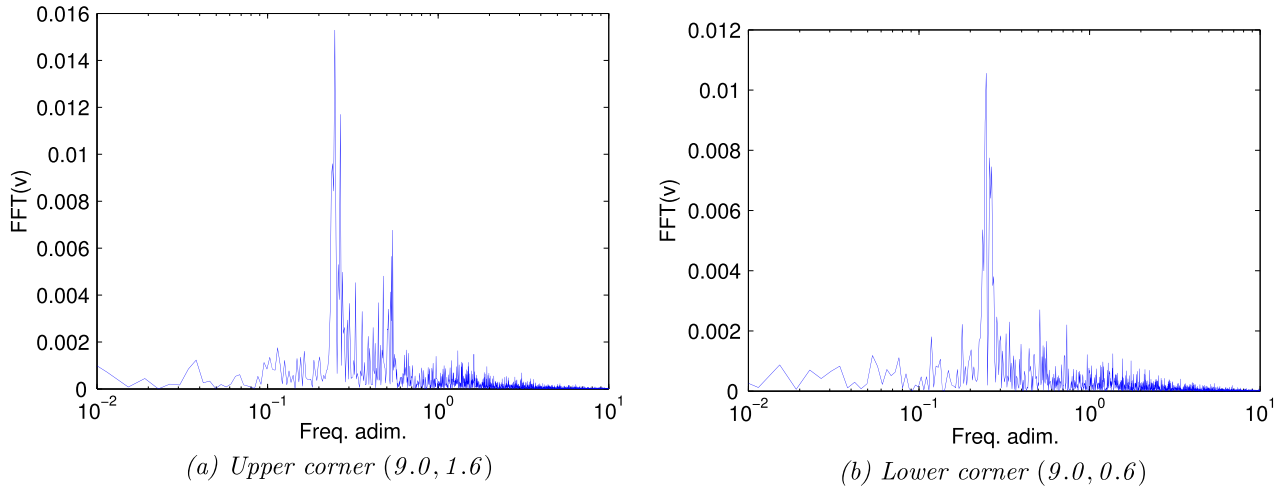

(b) Lower corner $(9.0, 0.6)$

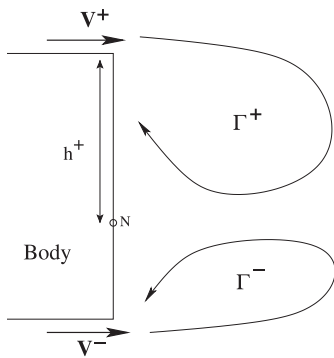**Fig. 6.** Spectrum of the vertical velocity component at the two corner points.

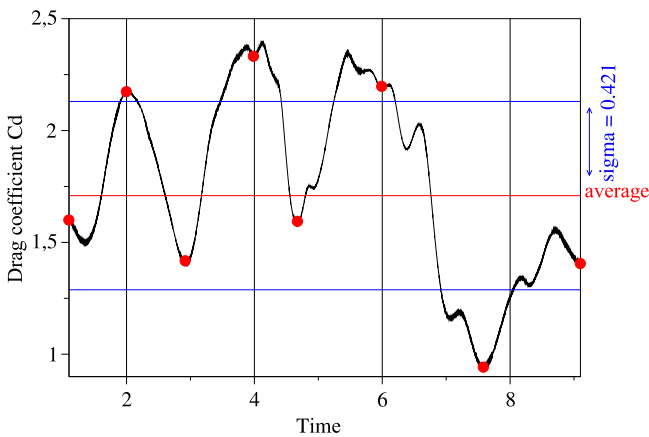**Fig. 7.** Diagram for the resolution of the Kolmogorov frequency.

Fig. 8. C_d history during two shedding cycles.

experimental and numerical studies concerning flows past bluff-bodies [22,21,25].

To characterize the pumping frequency, we use the Kolmogorov frequency $f_k = \frac{V^+}{h^+}$, where V^+ and h^+ are defined in Fig. 7. Searching the location of the attachment point N during time, we obtain $f_k = 0.16$ which corresponds to a Strouhal number (based on the mean value of h^+ and on the mean velocity at the point $(9.0, 1.6)$) of $St_k = 0.09$. This value is close to those obtained with LES numerical studies [23] and experiments [13]. It shows again that the

present simulations give physically realistic results as the small scales are well captured.

An efficient way to understand the impact of the flow behaviour on the body forces is to plot the C_d versus the time for two consecutive shedding cycles in the near wake (Fig. 8) and to explore the correlations between the dynamical evolution of the flow and the variations of the drag coefficient. As about two thirds of the drag forces are on the back wall, the discussion focus on this part of the flow. The pressure and the vorticity fields are plotted at different times corresponding approximately to local extrema of the drag coefficient representing the main evolution steps in the wake dynamics: vortex creation, development, emission and convection. As the Figs. 9 and 10 show counter-rotating vortices are alternatively generated at the lower and upper corners of the body as observed in the experiments reported in [28]. The lowest C_d value corresponds to a shedding moment when the core of the vortical structures is farther to the obstacle ($t = 7.6$) and the new structures are not yet formed. Oppositely, the highest C_d values occur when the shedded vortices strongly interact with the body ($t = 2$, 4, and 6).

4. Active control with blowing jets

It is chosen a priori to use only blowing set-ups in order to respond to some technical constraints of car industry. The thickness of the jets corresponds to the height of three cells that is equivalent to $h_j = 0.024$ on the finest grid. Four average amplitudes are used for the jets: $U_j = A\, U_\infty$, where the amplitude A takes the values 0.15, 0.3, 0.6, and 0.9 which correspond respectively to the forcing intensities C_μ: 5×10^{-4}, 2×10^{-3}, 8×10^{-3}, and 1.8×10^{-2}.

As we observed in the previous section, lower values of C_d are achieved when the wake vortex cores are away from the body. So, to take advantage of this property an active control with blowing jets should put away vortex structures, decreasing the drag forces. Fig. 1 shows the three locations selected for the blowing jets in the middle, the upper and the lower part of the square back wall. The upper and lower jets are located at the distance $H/3$ from the corners. In this section, three different active control approaches are studied. The first control consists in using blowing steady jets. The second control corresponds to using pulsed jets with a relevant frequency. The last control is a closed-loop procedure using sensors to capture the shedding frequency and adapt the blowing to it. The sensors are located at the distance of $H/10$ from the corners. In the following we refer to the uncontrolled case as case 0.

To choose the best amplitude of the jet in terms of energy saving, we use the non dimensional efficiency ξ taken as the ratio
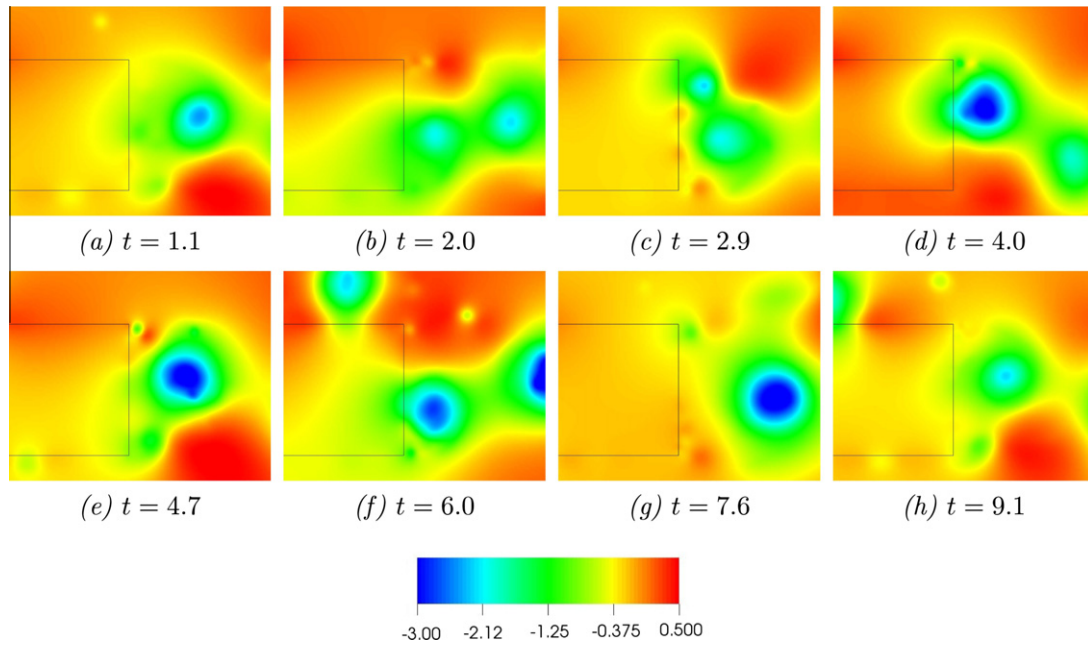
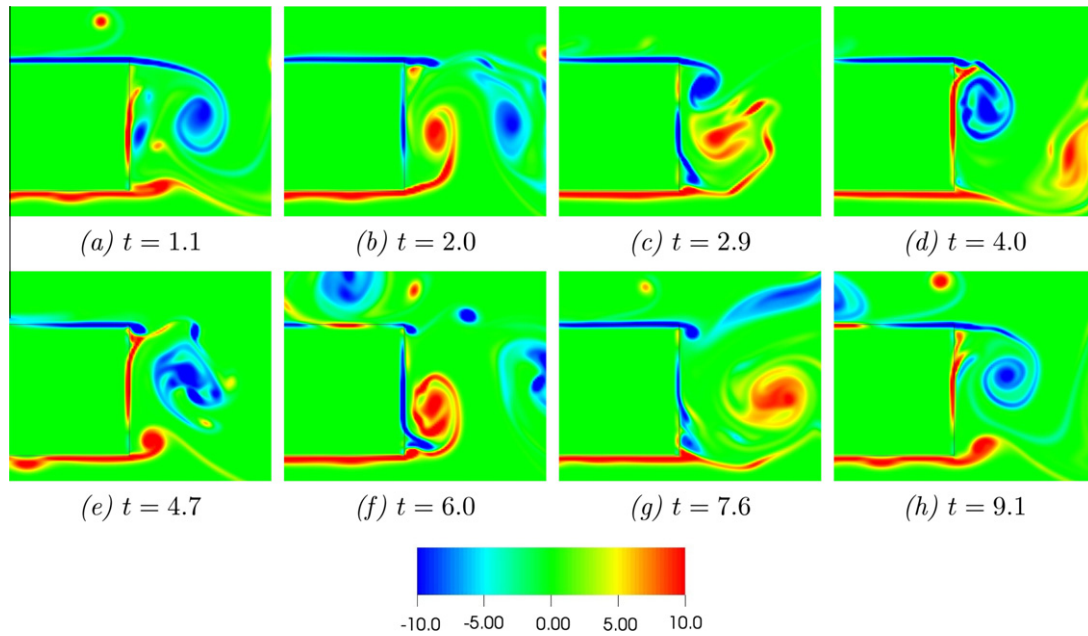**Fig. 9.** Evolution of the pressure field during two shedding cycles.

Fig. 10. Evolution of the vorticity field during two shedding cycles.

between the effective gain and the total power, where the effective gain is given by the improvement obtained on the drag coefficient minus the power necessary for the actuator

$$\xi = \frac{P_{saved} - P_{actuator}}{P_{total}} = -\frac{HU_\infty^3 \Delta(C_d) + h_j U_j^3(K_p + 1/\eta_{actuator})}{h_j U_j^3(K_p + 1/\eta_{actuator}) + HU_\infty^3 C_d/\eta_{engine}} \quad (5)$$

where P denotes the power, the subscript *saved* corresponds to the variation of power with respect to the uncontrolled case, the subscript *actuator* stands for the power related to the actuator only, the subscript *total* indicates the whole power (body aerodynamics and actuator) is taken into account, $\Delta(C_d)$ is the variation of the drag coefficient, K_p the pressure drop coefficient (set to 1 for a sudden

expansion) and η the efficiency of the jet mechanism or of the engine (generally set to 30% for a car engine and also used here for the actuator). If this coefficient is positive, the control is efficient and the greater it is, more efficient the control is.

4.1. Active control with steady jets

To explore the efficiency of this control, we need to study the effect of the jet position and its amplitude on the body drag coefficient.

Taking a steady jet U_j at the middle of the wall, a parameter study on the amplitude is performed. As the Table 1 shows the best result is obtained for the highest amplitude. However the gain

Table 1
Mean drag coefficients for the active control using steady jets.

Case	$C_{d_{up}}$	Var. $C_{d_{up}}$ (%)	$C_{d_{down}}$	Var. $C_{d_{down}}$ (%)	C_d	Var. C_d (%)
0	0.565	–	1.104	–	1.708	–
$J_{middle}(U_j = 0.15\ U_\infty)$	0.555	−2	1.103	−0	1.695	−1
$J_{middle}(U_j = 0.3\ U_\infty)$	0.526	−7	1.038	−6	1.590	−7
$J_{middle}(U_j = 0.6\ U_\infty)$	0.473	−16	0.854	−23	1.353	−21
$J_{middle}(U_j = 0.9\ U_\infty)$	0.447	−21	0.841	−24	1.314	−23
$J_{down}(U_j = 0.6\ U_\infty)$	0.526	−7	1.064	−4	1.616	−5
$J_{up}(U_j = 0.6\ U_\infty)$	0.486	−14	0.920	−17	1.445	−15
$J_{two-jets}(U_j = 0.6\ U_\infty)$	0.447	−21	0.815	−26	1.301	−24

Table 2
Efficiency of the active control using steady jets.

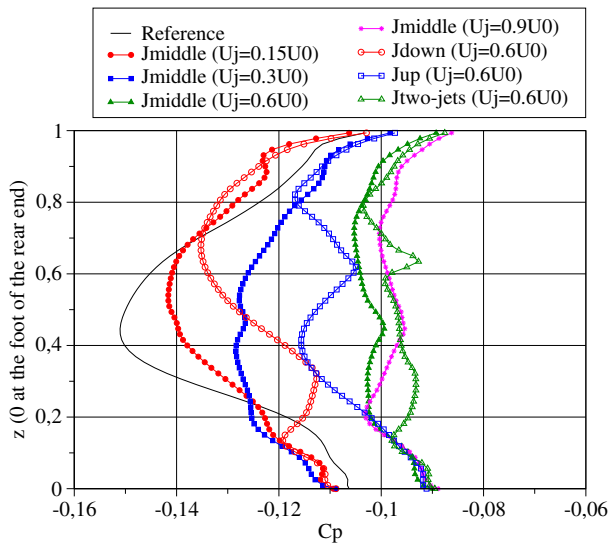| Case	$J_{middle}(0.15\ U_\infty)$	$J_{middle}(0.3\ U_\infty)$	$J_{middle}(0.6\ U_\infty)$	$J_{middle}(0.9\ U_\infty)$
ξ (%)	2	15	41	31

Fig. 11. C_p profile at the rear end of the body for the active control using steady jets.

Table 3
$C_{p_{min}}$ values and locations in the wake (the center of the back is the point (8.925, 1.1)) for the active control using steady jets.

Case	$C_{p_{min}}$	Var. $|C_{p_{min}}|$ (%)	x	z
0	−0.267	–	9.38	1.08
$J_{middle}(U_j = 0.15\ U_\infty)$	−0.268	−0	9.34	1.09
$J_{middle}(U_j = 0.3\ U_\infty)$	−0.236	−12	9.33	1.06
$J_{middle}(U_j = 0.6\ U_\infty)$	−0.202	−24	9.39	1.06
$J_{middle}(U_j = 0.9\ U_\infty)$	−0.192	−28	9.39	1.06
$J_{down}(U_j = 0.6\ U_\infty)$	−0.261	−22	9.34	1.14
$J_{up}(U_j = 0.6\ U_\infty)$	−0.216	−19	9.34	1.05
$J_{two-jets}(U_j = 0.6\ U_\infty)$	−0.191	−28	9.39	1.06

improvement between $A = 0.6$ and $A = 0.9$ is low and the best efficiency is achieved for $A = 0.6$ (Table 2). This amplitude will be used for the other tests of this sub section as, when the amplitude is small ($A = 0.15$ or $A = 0.3$), there is no significant modification of the drag forces. It appears that to be efficient the jet must reach a significant value of the velocity.

Then the effect of the wall jet location on the drag forces is studied. As shown in Table 1 the best result is obtained for a jet placed on the middle of the body (−21%). Let us note that the active control at the back induces a significant reduction of the pressure drag coefficient both in front and behind the body. Finally, a double jet configuration with two jets located at a distance $H/3$ from the corners of the back wall is also studied. This control does not improve significantly the drag reduction compared to one jet at the middle.

The correlation between the pressure in the wake and the drag coefficient can be noticed in Fig. 11 representing the C_p values at the rear wall of the body and in the Table 3 giving the minimum and the location of the static pressure coefficient in the wake. The best cases for the drag reduction ($U_{j_{middle}} = 0.6\ U_\infty$, $U_{j_{middle}} = 0.9\ U_\infty$ and $U_{j_{two-jets}} = 0.6\ U_\infty$) are reached for the highest values of C_p and $C_{p_{min}}$ at the back. So, the decrease of the drag forces is strongly linked to the decrease of the wake depression behind the body back. Let us note that the distance to the body of the depression center (x values in Table 3) is similar for all cases. However, the distance to the road changes with the position of the actuator; specially when the jet is in the lower part of the body as the depression center moves away from the road. One can observe on the C_p isolines (Fig. 12 compared to Fig. 5) that the control jet (with $U_{j_{middle}} = 0.6\ U_\infty$) decreases significantly the C_p gradients in the wake. In addition the vorticity isolines are less concentrated behind the back wall.

Another interesting issue is to see the impact of the control to the shedding. It appears that the main frequency $f = 0.29$ (instead of $f = 0.25$) is increased (Fig. 13) and so is the Strouhal number $St = 0.30$ (instead of $f = 0.22$). The change on the Kolmogorov frequency $f_k = 0.30$ and its related Strouhal number $St_k = 0.23$ is much more drastic.

Finally, as in the previous section, we explore the link between the flow evolution and the drag coefficient. The history of the drag coefficient during a shedding cycle is plotted in Fig. 14. Four times corresponding to the extrema and the mean value are selected but this mean value is close to 1.3 when the mean value of the uncontrolled case is about 1.7. The plots in Figs. 15 and 16 show clearly that the alternation of big vortical structures (Figs. 9 and 10) is
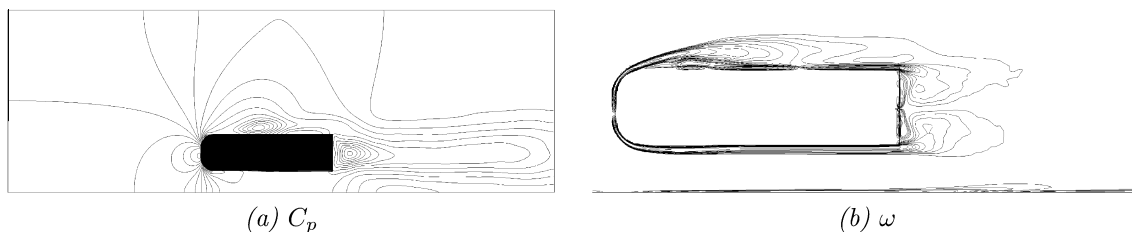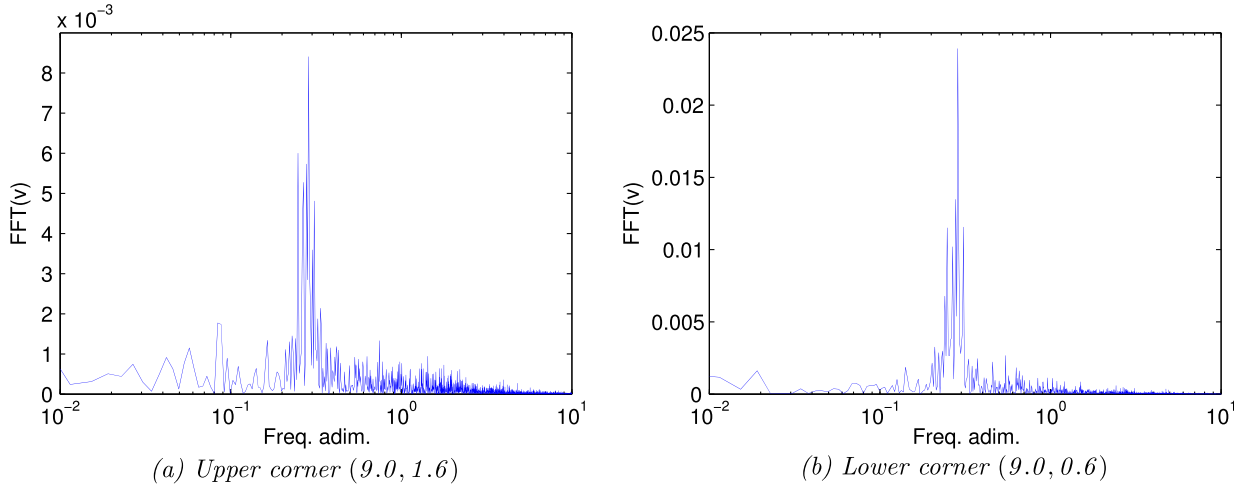

(a) C_p (b) ω

Fig. 12. Mean C_p and vorticity fields for the active control using a middle steady jet with $U_j = 0.6\ U_\infty$.

Fig. 13. Spectra of the vertical velocity component for the active control using a middle steady jet with $U_j = 0.6\, U_\infty$.
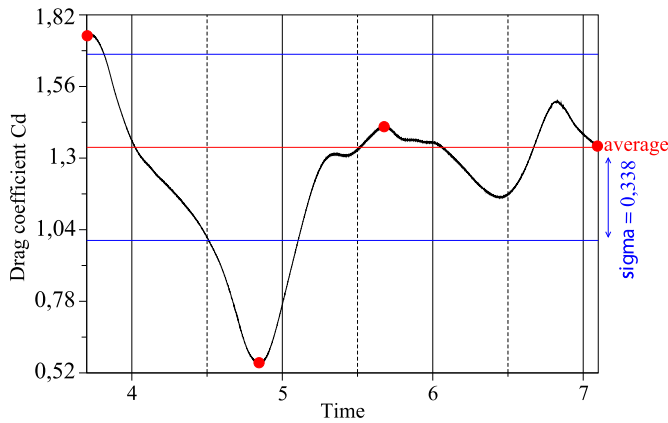

Fig. 14. C_d history during a shedding cycle for the active control using a middle steady jet with $U_j = 0.6\, U_\infty$.

replaced by a more chaotic shedding of smaller vortices, especially on the top, where the flow is weaker than at the bottom due to the presence of the road. There is no more deep wells of pressure either in the near wake.

4.2. Active control with pulsed jets

The pulsed jets (open loop) control is based on a periodical blowing actuator with the same thickness h_j than for the steady jet. The actuator blows between zero and $U_{jmax} = A\, U_\infty$ with the following law

$$U_j = \frac{U_{jmax}}{2}[1 - cos(2\pi f_j t)] \qquad (6)$$

where the frequency $f_j = 0.5$ corresponds to the double frequency of the uncontrolled shedding. The formula (6) means that the mean velocity of the jet is $\overline{U_j} = U_{jmax}/2$ and the maximum velocity of the jet is U_{jmax}. An interesting question is to know if the important point is the mean value or the maximum of the jet velocity. In Tables 4, 5, and Fig. 17, we see that $\overline{U_j} = 0.3\, U_\infty$ and $\overline{U_j} = 0.6\, U_\infty$ give very different values as in the steady case. So it seems that the mean velocity is more determinant than the maximum of velocity contrarily to what we thought. Indeed as the shedding frequency is around 0.25, there is a big vortex just behind the back wall with a double frequency around 0.5 and so it is necessary to blow strongly at these events. When $\overline{U_j} = 0.3\, U_\infty$, the maximum of the jet velocity is 0.6 (as for the steady jet) that occurs when the strong vortices behind the body are close to the back wall but the result show that it is not enough. In addition, it is also required to adjust the phase in order the maximum of blowing occurs at the right time. If the jet is not synchronized to the flow (that means the maximum blowing occurs when the drag forces are low) the drag reduction is very low. In conclusion, when the action is synchronized to the flow (when the maximum blowing occurs with the maximum of the drag forces) a good control is achieved with a mean jet of 0.6 as for the steady jet.

The C_p profiles at the rear end of the body (see Fig. 17) show that the behaviour is about the same for the two values of $\overline{U_j}$ but there
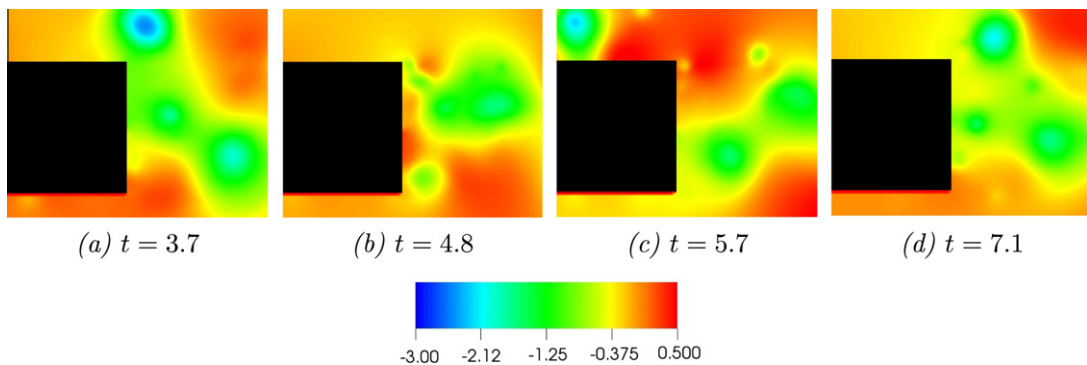

Fig. 15. Evolution of the pressure field during a shedding cycle for the active control using a middle steady jet with $U_j = 0.6\, U_\infty$.
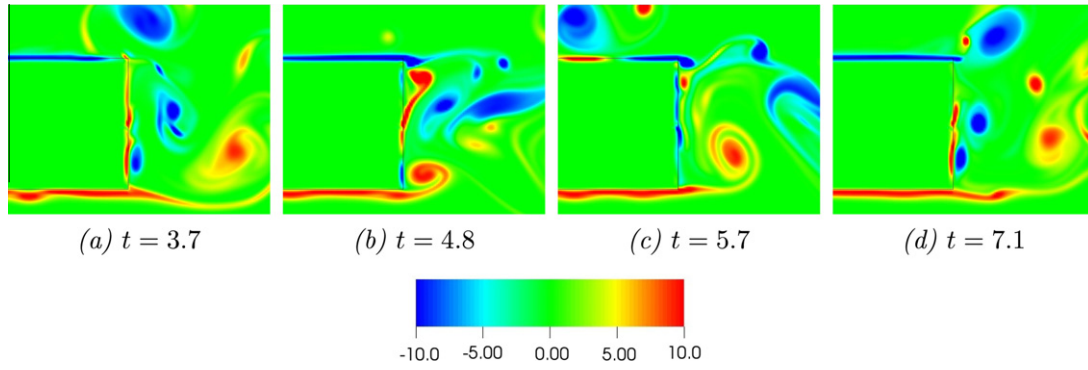
Fig. 16. Evolution of the vorticity field during a shedding cycle for the active control using a middle steady jet with $U_j = 0.6\ U_\infty$.

Table 4
Mean drag coefficients for the active control using pulsed jets.

Case	$C_{d_{up}}$	Var. $C_{d_{up}}$ (%)	$C_{d_{down}}$	Var. $C_{d_{down}}$ (%)	C_d	Var. C_d (%)
0	0.565	–	1.104	–	1.708	–
$J_{middle}(\overline{U_j} = 0.3\ U_\infty)$	0.539	−5	1.078	−2	1.656	−3
$J_{middle}(\overline{U_j} = 0.6\ U_\infty)$	0.460	−19	0.880	−20	1.380	−19
$J_{two-jets}(\overline{U_j} = 0.6\ U_\infty)$	0.486	−14	0.933	−15	1.459	−15

Table 5
$C_{p_{min}}$ values and locations in the wake (the center of the back is the point $(8.925, 1.1)$) for the active control using pulsed jets.

Case	$C_{p_{min}}$	Var. $|C_{p_{min}}|$ (%)	x	z
0	−0.267	–	9.38	1.08
$J_{middle}(\overline{U_j} = 0.3\ U_\infty)$	−0.251	−6	9.33	1.11
$J_{middle}(\overline{U_j} = 0.6\ U_\infty)$	−0.203	−24	9.39	1.09
$J_{two-jets}(\overline{U_j} = 0.6\ U_\infty)$	−0.214	−20	9.38	1.08

Fig. 17. C_p profile at the rear end of the body for the active control using pulsed jets.

is a significant reduction when the blow is stronger. The results obtained with $\overline{U_j} = 0.6\ U_\infty$ are very close to those observed for the steady jet as shown in Fig. 18. However the shedding frequency is less clear at the upper corner (Fig. 19) but is about the same for the lower corner with $f = 0.27$. It seems that the upper vortex is partly destroyed, whereas the lower corner remains very strong as illustrated on the snapshots of the pressure and vorticity fields (Figs. 21 and 22) corresponding to particular points of the drag history (Fig. 20).

A last simulation is performed at $\overline{U_j} = 0.6\ U_\infty$ with two pulsed jets located at 1/3 and 2/3 of the height with a frequency 0.25 corresponding to the global shedding. Each jet is synchronized to the corresponding vortex of the uncontrolled flow. The upper jet has a maximum blowing when the upper vortex is formed and located in front and at the same time the lower jet does not blow. Of course the cost of the action is doubled as there are two jets but unfortunately the results are not better than those obtained with a single jet as shown in Tables 4, 5, and Fig. 17.

4.3. Closed-loop active control

The closed-loop control is based on the pressure variations at the back as there is a strong decrease of the pressure on the wall when a big structure is generated. Therefore, it is necessary to add a sensor to measure the pressure on the back wall. The actuator with the same thickness h_j than for the steady jet blows with the following law

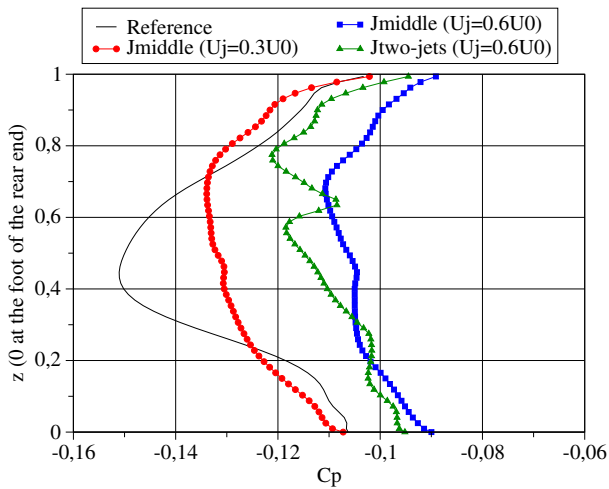$$U_j = \frac{U_{jmax}}{2}[1 - \beta(p_{sensor} - \bar{p}_{sensor})]\tag{7}$$
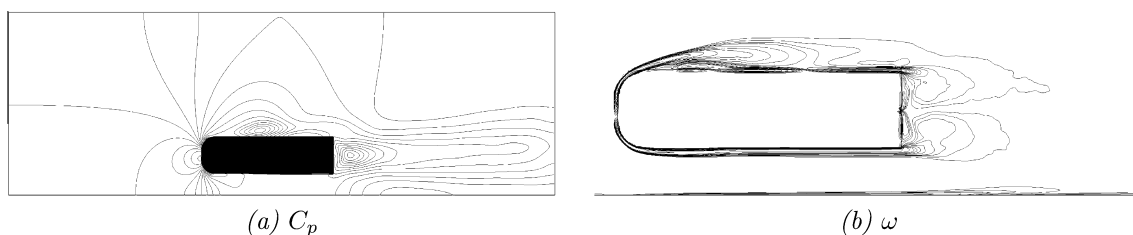

Fig. 18. Mean C_p and vorticity fields for the active control using one pulsed jet with $\overline{U_j} = 0.6\ U_\infty$.
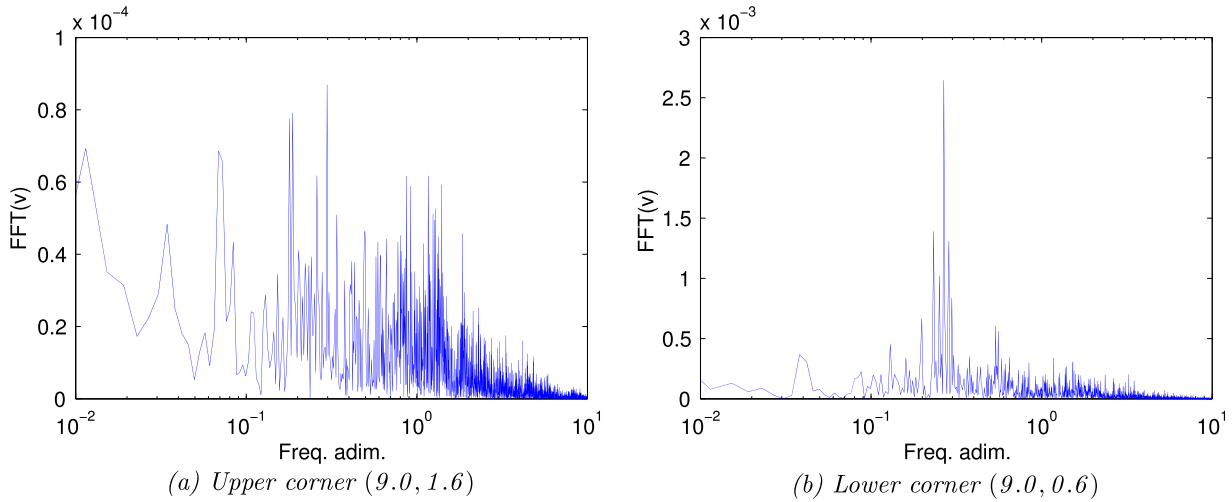
Fig. 19. Spectra of the vertical velocity component for the active control using one pulsed jet with $\overline{U_j} = 0.6\, U_\infty$.
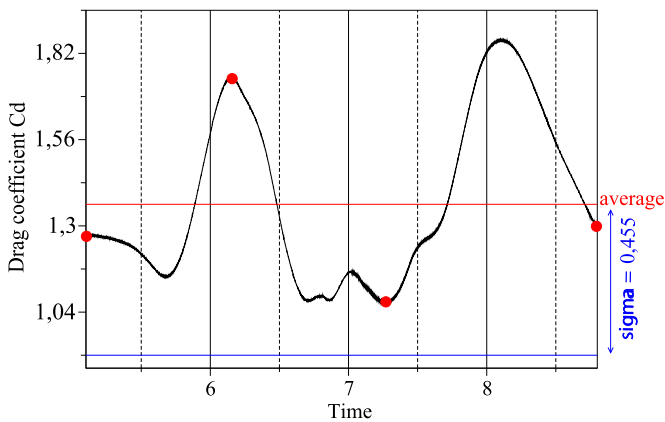

Fig. 20. C_d history during a shedding cycle for an active control using one pulsed jet with $\overline{U_j} = 0.6\, U_\infty$.

where $U_{jmax} = 1.2$ induces $\overline{U_j} \approx 0.6 U_\infty$, p_{sensor} is the pressure read by the sensor, $\bar{p}_{sensor}$ is the mean pressure at the sensor and β is a normalized coefficient which allows to force the blowing to reach the extrema 0 and U_{jmax}. The value of $\bar{p}_{sensor}$ is not set a priori but is updated all along the simulation. In addition the slope of the function $U_j(t)$ along time is limited to one in order to avoid the instabilities due to abrupt pressure changes in the wake. The advantage of the closed-loop compared to the pulsed jet is that there is no problem

of synchronisation with the flow as the flow itself regulates the action.

Three cases are studied with the actuator in the middle and the pressure measured at one sensor on the top part, one sensor on the bottom part or two sensors (Fig. 1). In this last case $p_{sensor} = min(p_{sensor1}, p_{sensor2})$ and $\bar{p}_{sensor} = 0.5(\bar{p}_{sensor1} + \bar{p}_{sensor2})$ to take into account the presence of a vortex in the vicinity of one of the sensors. The results obtained with one single sensor are slightly lower than for the pulsed case as shown in Tables 6, 7, and Fig. 23. But using the two sensors we can reach a 20% drag reduction. The main advantage of the close-loop active control is the action is automatically fitted to the shedding. For the pressure field in the wake, the remarks are the same than for the control with steady jet (Fig. 23 and Table 7). The most the depression is limited in space and in C_p values, the most the drag coefficient decreases. Indeed, the case with the two sensors corresponds to the highest value of the $C_{p_{min}}$ and also to the best reduction of the C_d. For the rest of the closed-loop active control study, only this control case is detailed. These drag and pressure results are in good agreement with those obtained by Pastoor et al. in [28].

Once again the mean flow is very similar to those observed for the two previous active controls (Fig. 24). The shedding frequency in the upper corner is close to 0.3 but no shedding frequency is found in the lower corner (see Fig. 25). Once again, the snapshots of the solution at various time of the shedding (Fig. 26) show that the drag coefficient is strongly linked to the pressure drag induced by the strong vortices at the back, especially the lower one (Figs. 27 and 28). The C_d oscillations visible in Fig. 26 are due to the quick
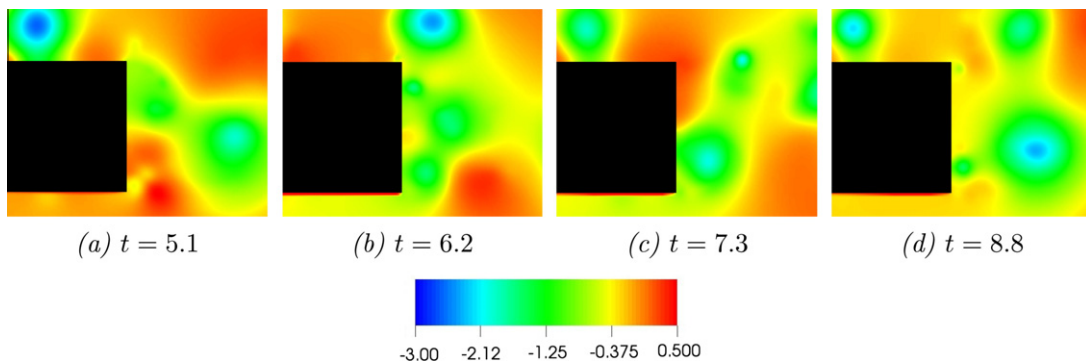

Fig. 21. Evolution of the pressure field during a shedding cycle for an active control using one pulsed jet with $\overline{U_j} = 0.6\, U_\infty$.
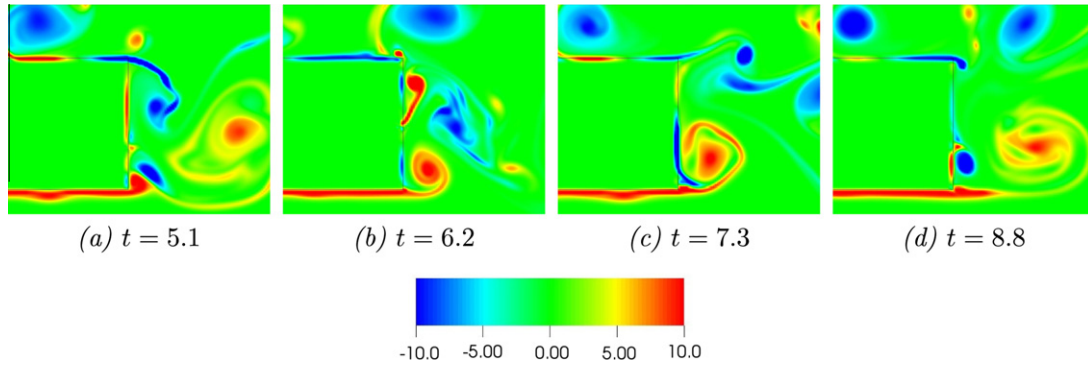
Fig. 22. Evolution of the vorticity field during a shedding cycle for an active control using one pulsed jet with $\overline{U_j} = 0.6 \, U_\infty$.

Table 6
Mean drag coefficients for the closed-loop active control.

Case	$C_{d_{up}}$	Var. $C_{d_{up}}$ (%)	$C_{d_{down}}$	Var. $C_{d_{down}}$ (%)	C_d	Var. C_d (%)
0	0.565	–	1.104	–	1.708	–
$J_{middle}(S_{up})$	0.486	−14	0.920	−17	1.432	−16
$J_{middle}(S_{down})$	0.499	−12	0.972	−12	1.498	−12
$J_{middle}(S_{both})$	0.473	−16	0.867	−21	1.367	−20

Table 7
$C_{p_{min}}$ values and locations in the wake (the center of the back is the point (8.925,1.1)) for the closed-loop active control.

Case	$C_{p_{min}}$	Var. $|C_{p_{min}}|$ (%)	x	z
0	−0.267	–	9.38	1.08
$J_{middle}(S_{up})$	−0.216	−19	9.38	1.08
$J_{middle}(S_{down})$	−0.218	−18	9.39	1.11
$J_{middle}(S_{both})$	−0.195	−27	9.38	1.06
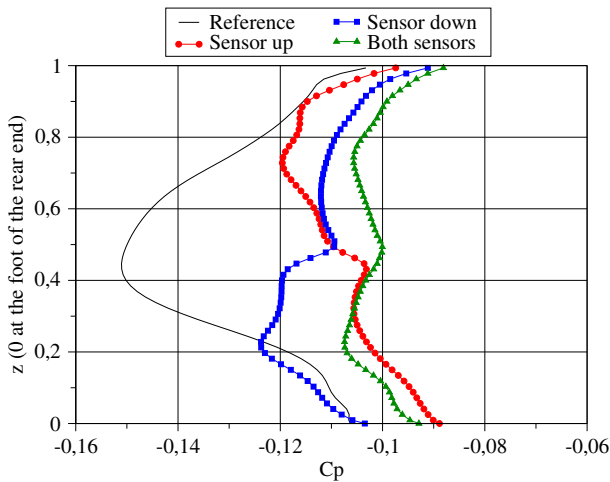
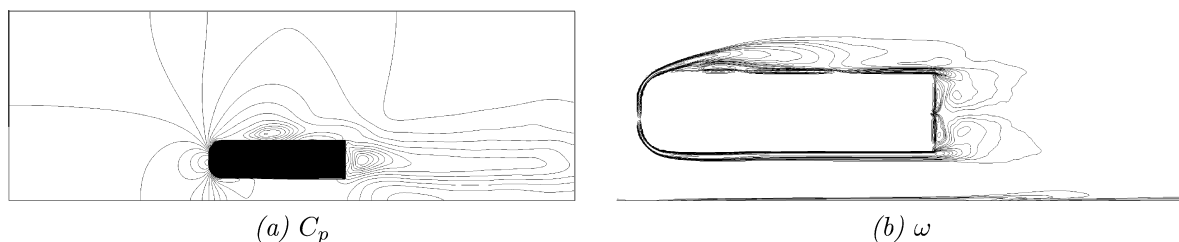Fig. 23. C_p profile at the rear end of the body for the closed-loop active control.

evolution of the pressure near the actuators. That is why a time slope is used to limit this unstable effect.

5. Passive control using porous layers

A control using porous layers is widely studied in [6] for the square back Ahmed body on top of a road. The main difference with the previous study is the distance between the body and the road that is equal to H in [6] and to $0.6H$ here as in the original benchmark [2]. The closer the body is to the road the more important the jet effect under the body is. In this section, the study is focused on two efficient geometries (Fig. 29) corresponding to the cases giving the best drag reductions in [6].

It should be noted that the distance to the road modifies the efficiency of the passive control. According to the Table 8, the drag reduction is altered when the body is closer to the road as the velocity of the jet flow under the body is conversely proportional to this distance. Therefore it is more difficult to control the bottom shedding. Nevertheless, the decrease of the drag coefficient (more than 20%) is still high. In Fig. 30, the profiles show clearly that the C_p values are strongly increased. It is directly linked to the drastic reduction of $C_{d_{down}}$ that corresponds to the reduction of the near wake pressure forces. This result is confirmed by Table 9, where a drastic improvement of the $C_{p_{min}}$ compared to the uncontrolled case is observed.

As the Figs. 31 and 32 show, the back vortex for the case 2 contains low intensity pressure and vorticity fields compared to the case 1. These figures confirm also that the distance of the structures centers from the wall is correlated to the down drag
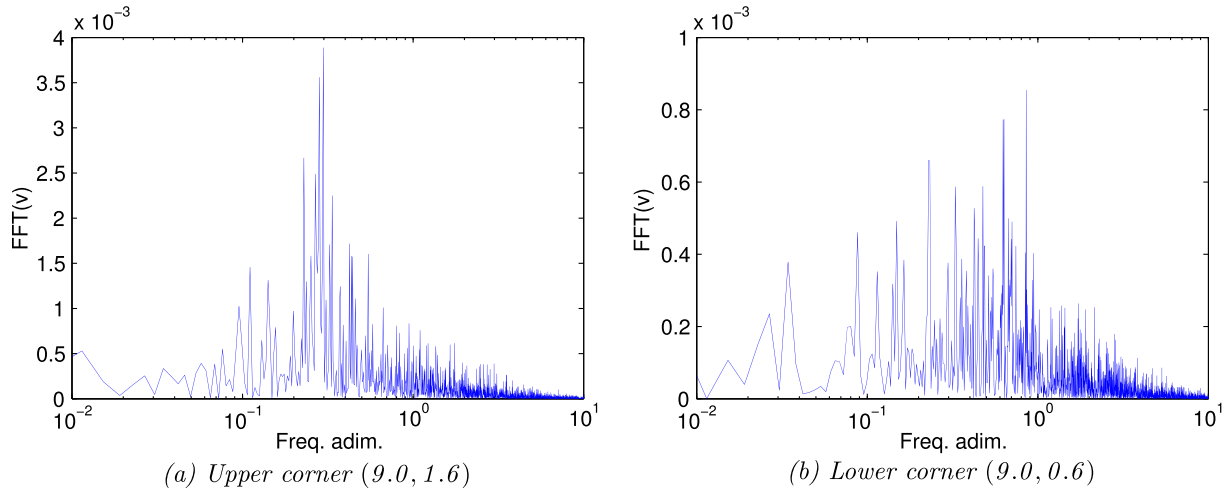

Fig. 24. Mean C_p and vorticity fields for the closed-loop active control with both sensors.

(a) Upper corner $(9.0, 1.6)$　　　　*(b) Lower corner $(9.0, 0.6)$*

Fig. 25. Spectra of the vertical velocity component for the closed-loop active control with both sensors.
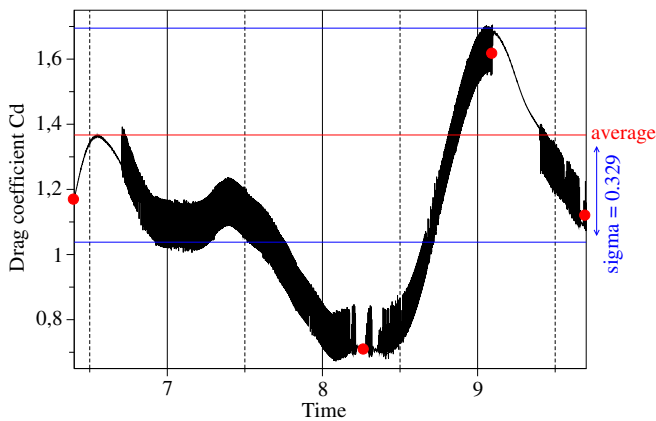

Fig. 26. C_d history during a shedding cycle for the closed-loop active control with both sensors.

coefficient decrease. In front, the porous corners induce a transverse jet and as a consequence the recirculation zone increases and so the up drag coefficient (see [6] for more details). Thus, despite the drastic improvement of the down drag coefficient for case 2, the total drag coefficients are close to each other.

The vertical velocity spectra are plotted for the cases 1 and 2 in the Fig. 33. There is no more a dominant frequency around 0.25. Indeed, as the Figs. 36 and 38 show the porous layers modify com-

pletely the shear forces along the body and then the vortex shedding is very different from case 0. For case 1 there is a porous layer only on top of the body and we can see that the big vortices in the shedding zone are replaced by small structures but the bottom vortices are still present. For case 2, there are small vortices on both sides, specially at the bottom wall as small vortices are reinforced by the jet under the body. Indeed, introducing porous layers induces a low velocity flow in the porous medium parallel to the main flow in the fluid. At the interface between these two flows there is a Kelvin-Helmholtz instability that yields small vortices that are clockwise on top of the body (blue in the figures) and counter clockwise below. These small vortices, that replace the uncontrolled large structures, are convected to the back and change drastically the flow behaviour, participating to a very strong decrease of the down drag coefficient (Table 8). The pressure fields (Figs. 35 and 37) reveal that the pressure is much higher than for the uncontrolled case. The wells centers are further to the body and have very few influence on the body wall itself as seen in Fig. 30, where the C_p is almost constant at -0.08 all along the wall. The plot (d) of Figs. 35 and 37 that correspond to the higher values of the drag coefficient (Fig. 34) show a similar well close to the body. Nevertheless the origin is different, for case 1 it corresponds to a single vortex and for case 2 to the merging of three eddies.

In summary, the passive control using porous layers is very efficient, specially for the down drag coefficient. Putting a porous layer on the roof yields a 22% drag reduction due to the modification of the shear forces and the breaking of the shedding procedure. Adding a layer at the bottom is also very efficient to break the shedding
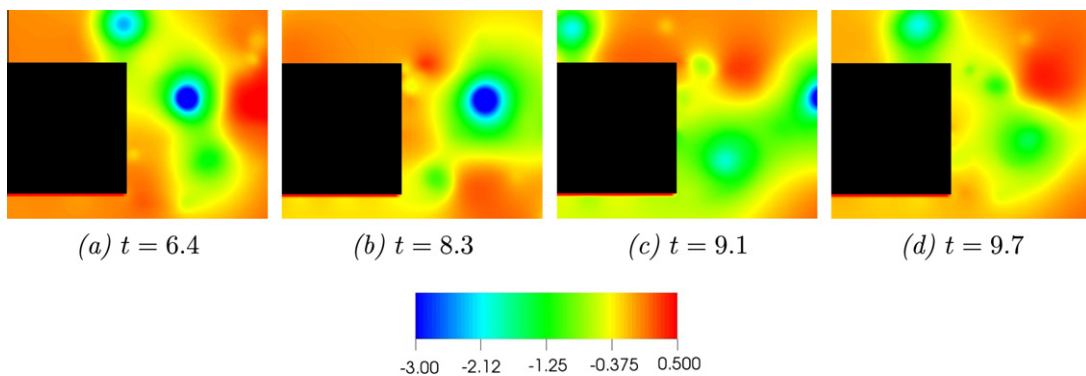

(a) $t = 6.4$　　　*(b) $t = 8.3$*　　　*(c) $t = 9.1$*　　　*(d) $t = 9.7$*

-3.00　　-2.12　　-1.25　　-0.375　　0.500

Fig. 27. Evolution of the pressure field during a shedding cycle for the closed-loop active control with both sensors.

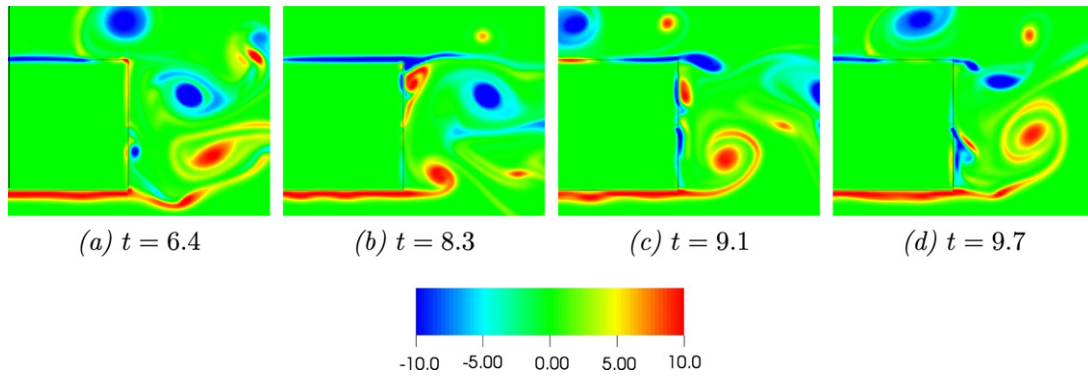(a) t = 6.4   (b) t = 8.3   (c) t = 9.1   (d) t = 9.7

-10.0   -5.00   0.00   5.00   10.0

Fig. 28. Evolution of the vorticity field during a shedding cycle for the closed-loop active control with both sensors.

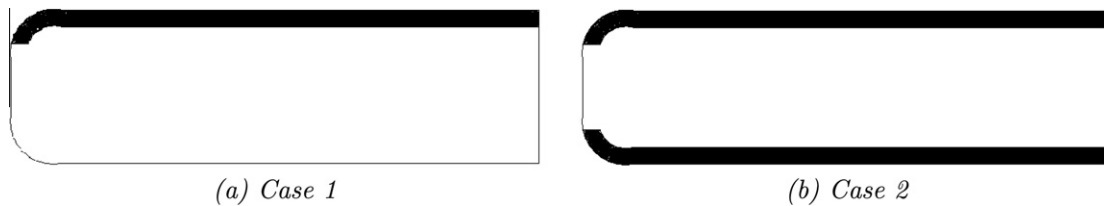(a) Case 1   (b) Case 2

Fig. 29. Porous layers configurations for the passive control.

Table 8
Mean drag coefficients for the passive control using porous layers.

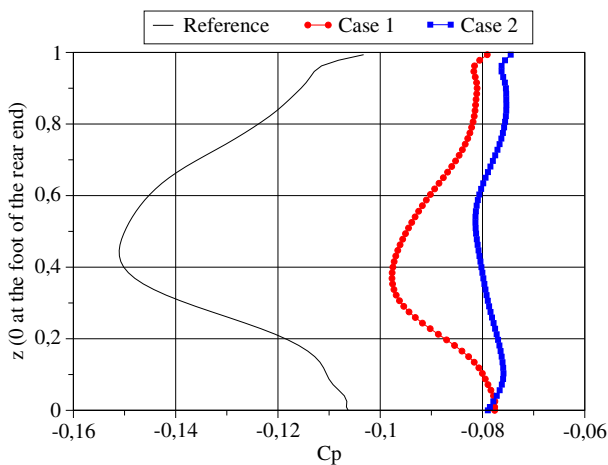| Case	$C_{d_{up}}$	Var. $C_{d_{up}}$ (%)	$C_{d_{down}}$	Var. $C_{d_{down}}$ (%)	C_d	Var. C_d (%)	Var. C_d from [6] (%)
0	0.565	–	1.104	–	1.708	–	–
1	0.604	+7	0.696	−37	1.327	−22	−37
2	0.683	+21	0.565	−49	1.275	−25	−31

Fig. 30. C_p profile at the rear end of the body for the passive control using porous layers.

Table 9
$C_{p_{min}}$ values and locations in the wake (the center of the back is the point $(8.925, 1.1)$) for the passive control using porous layers.

Case	$C_{p_{min}}$	Var. $|C_{p_{min}}|$ (%)	x	z
0	−0.267	–	9.38	1.08
1	−0.161	−40	9.33	1.00
2	−0.124	−54	9.42	1.08

but the significant increase of the up drag coefficient prevents from a drastic change.

6. Coupling passive and active control

The results obtained above are encouraging but somehow disappointing as it is difficult to determine a priori the effect of a control technique. For the active control, the closed-loop procedure is more adapted to the flow fluctuations and gives good results. Nevertheless, the efficiency is closely related to the location of the actuators and the sensors. The passive control gives very good results but the combination of the porous layer with the jet flow between the body and the road is not easy to understand and predict. In this section the coupling of passive and active control techniques is proposed. The choice is to keep a porous layer on the roof and to add an action at the bottom back to improve the efficiency. Keeping the porous layer yields a beneficial change of the shear forces along the roof and split the upper strong shedding vortex into smaller eddies. This is possible for the square back Ahmed body as there is no rear window and the result is a 22% reduction of the drag coefficient. We have seen in the previous section that the big bottom shedding vortex remains. It is thus necessary to make an action on it. Using a porous layer at the bottom is not efficient, so the idea is to use a closed-loop blowing jet to push it down in the wake. The position of this jet is at $H/3$ from the bottom corner that corresponds to the main position of the vortex center and the sensor is located at the down position (Fig. 1). First of all let us see the impact of such an active control alone on the flow behaviour. Curiously, the results are not very good (see the Tables 10
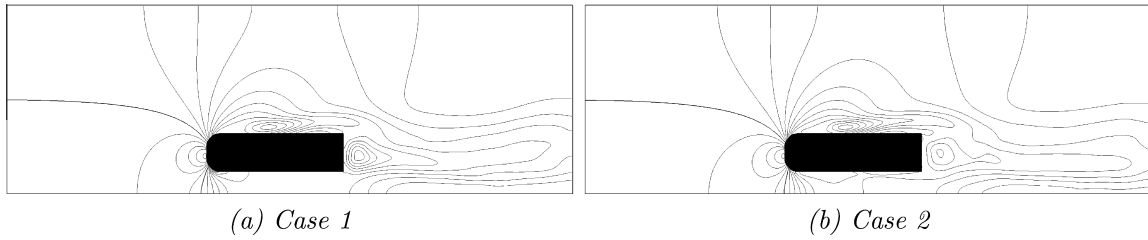
(a) Case 1　　　　　　　　　　　　　　　　　　　(b) Case 2

Fig. 31. Static pressure coefficient isolines for the passive control using porous layers.

(a) Case 1　　　　　　　　　　　　　　　　　　　(b) Case 2
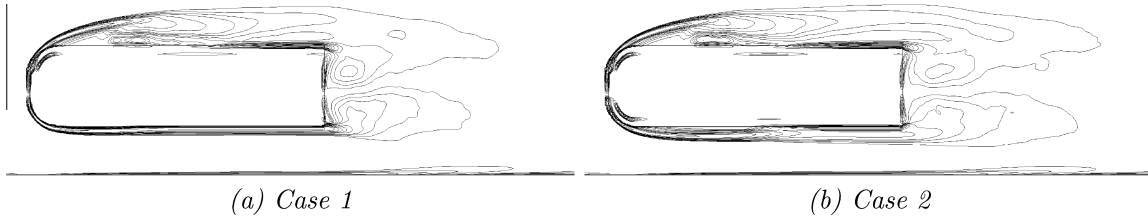
Fig. 32. Vorticity isolines for the passive control using porous layers.
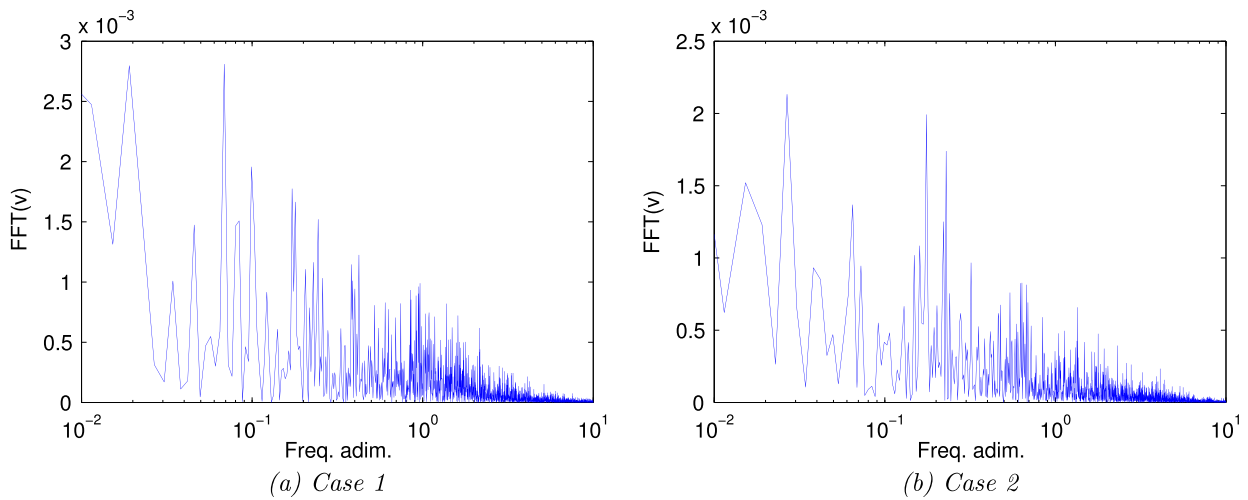

(a) Case 1　　　　　　　　　　　　　　　　　　　(b) Case 2

Fig. 33. Spectra of the vertical velocity component at point (9.0, 1.6) for the passive control using porous layers.

(a) Case 1　　　　　　　　　　　　　　　　　　　(b) Case 2
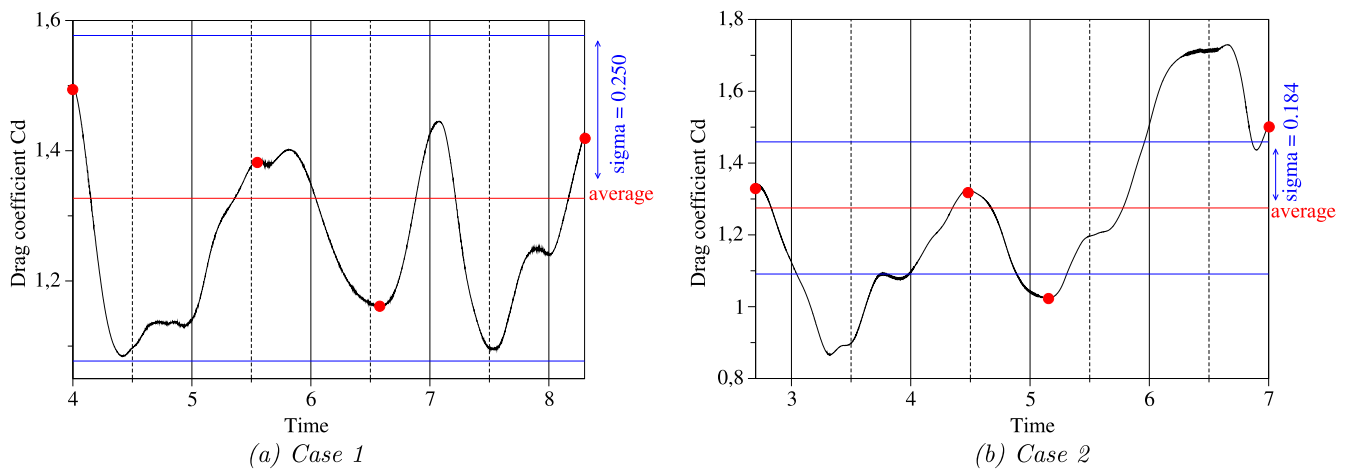
Fig. 34. C_d history during a shedding cycle of the uncontrolled case for the passive control using porous layers.

(a) t = 4.0   (b) t = 5.5   (c) t = 6.6   (d) t = 8.3

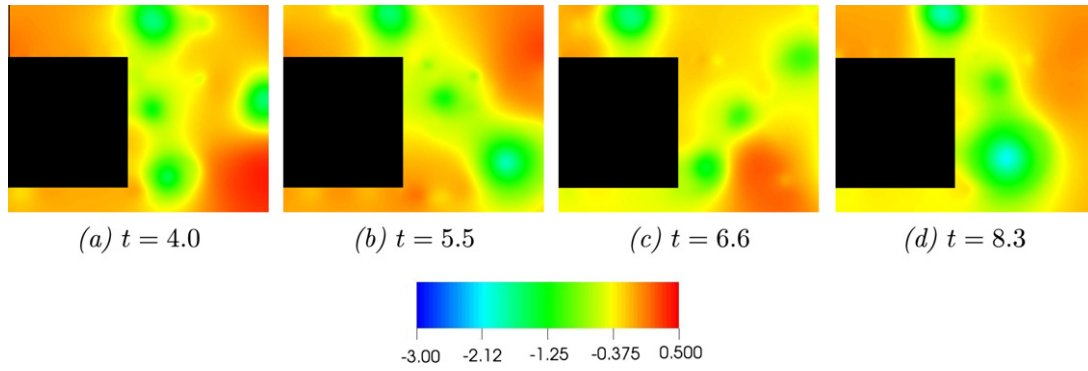-3.00   -2.12   -1.25   -0.375   0.500

Fig. 35. Evolution of the pressure field during a shedding cycle of the uncontrolled case for the porous passive control with one layer on top of the body (case 1).
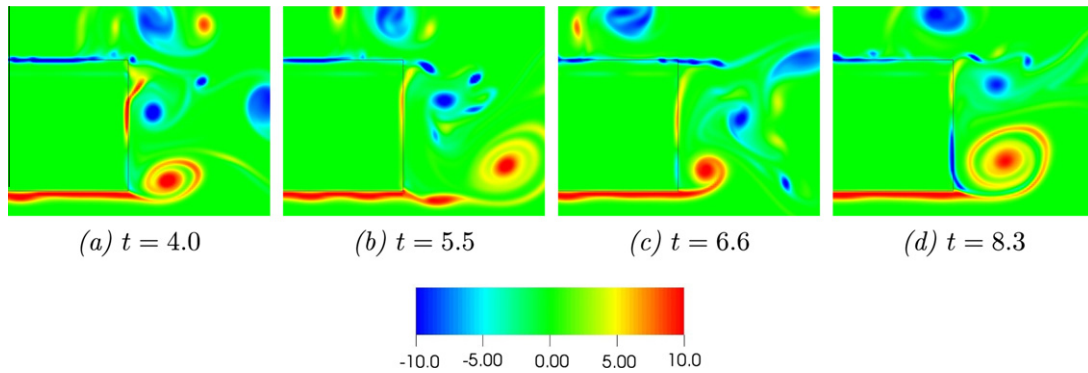

(a) t = 4.0   (b) t = 5.5   (c) t = 6.6   (d) t = 8.3

-10.0   -5.00   0.00   5.00   10.0

Fig. 36. Evolution of the vorticity field during a shedding cycle of the uncontrolled case for the porous passive control with one layer on top of the body (case 1).
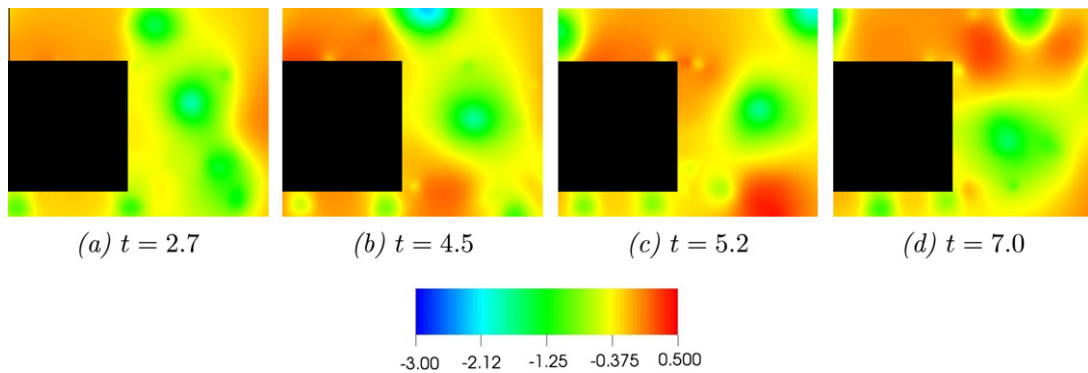

(a) t = 2.7   (b) t = 4.5   (c) t = 5.2   (d) t = 7.0

-3.00   -2.12   -1.25   -0.375   0.500

Fig. 37. Evolution of the pressure field during a shedding cycle of the uncontrolled case for the porous passive control with two layers (case 2).

(a) t = 2.7   (b) t = 4.5   (c) t = 5.2   (d) t = 7.0

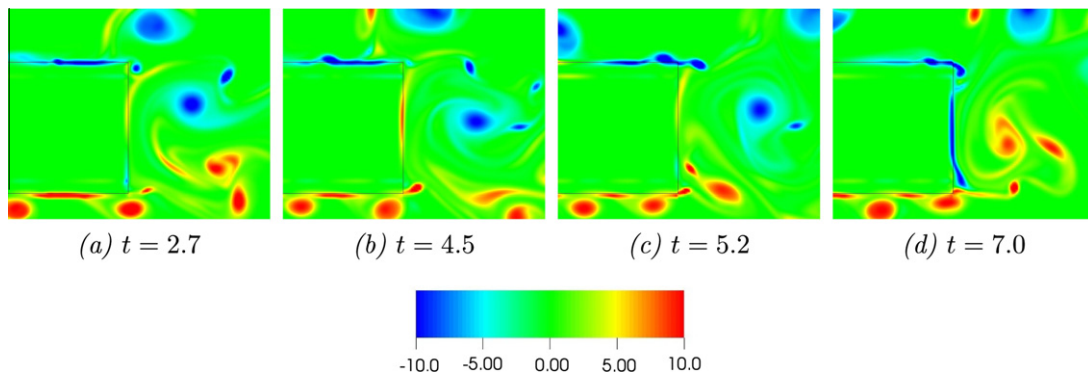-10.0   -5.00   0.00   5.00   10.0

Fig. 38. Evolution of the vorticity field during a shedding cycle of the uncontrolled case for the porous passive control with two layers (case 2).

Table 10
Mean drag coefficients for the passive control (case 1), the closed-loop active control at the down point and the coupled passive–active control.

Case	$C_{d_{up}}$	Var. $C_{d_{up}}$ (%)	$C_{d_{down}}$	Var. $C_{d_{down}}$ (%)	C_d	Var. C_d (%)
0	0.565	–	1.104	–	1.708	–
1	0.604	+7	0.696	−37	1.327	−22
J_{down}	0.539	−5	1.064	−4	1.629	−5
Coupled	0.552	−2	0.591	−46	1.183	−31

Table 11
$C_{p_{min}}$ values and locations in the wake (the center of the back is the point (8.925,1.1)) for the passive control (case 1), the closed-loop active control at the down point and the coupled passive–active control.

Case	$C_{p_{min}}$	Var. $|C_{p_{min}}|$ (%)	x	z
0	−0.267	–	9.38	1.08
1	−0.161	−40	9.33	1.00
J_{down}	−0.266	−0.4	9.34	1.14
Coupled	−0.131	−51	9.38	1.00

Fig. 41. C_d history during a shedding cycle for the coupled passive–active control.

and 11). This is probably due to the fact that the action of the upper vortex to the body is reinforced as the separation point between the mean vorticity isolines changes according to the position of the jet. Indeed, the decrease of the lower vortex facilitates the growing of the upper recirculation zone, so the global back wall underpressure zone does not decrease significantly (see the C_p profile in Fig. 44). The only fact to change the position of the actuator from the middle position to this new position changes the evolution of the drag coefficient from −12% (see Table 6) to −5% !

We decide now to couple both control procedures. The results are astonishing as the drag coefficient reduction reaches −31% that is better than 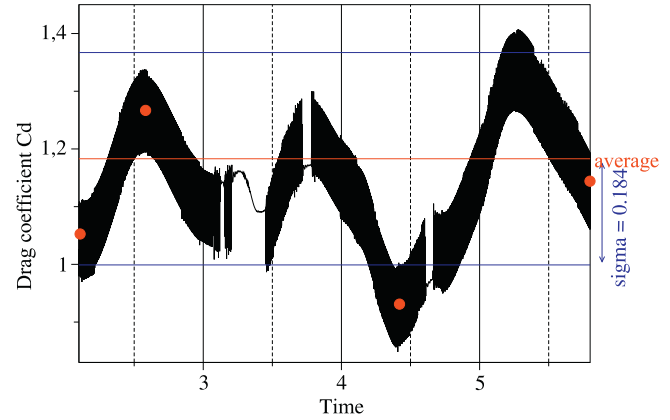the sum of the two gains and corresponds to our hopes. It is interesting to analyse carefully the impact of this coupled control on the flow behaviour. The Fig. 39 on the mean flow shows clearly that the mean flow is very close to those observed for the passive control (case 2) except the recirculation zone is not changed under the body and the bottom vortex is pushed away.

To complete the study let us look at the flow evolution during a shedding cycle of the uncontrolled case as the main frequency is not easy to determine (Fig. 40). The averaged drag coefficient is very low around 1.18 (Fig. 41). This is due to the fact that the vortex structures at the back are much smaller, on top due to the porous layer and at the bottom because the jet split the big vortex into smaller parts (see Figs. 42 and 43).

Finally, in Fig. 44 are plotted the C_p profiles at the rear end of the body for the uncontrolled case and the three above test cases. The
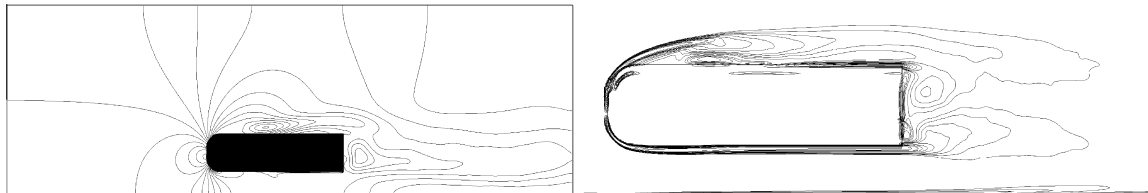

Fig. 39. Static pressure coefficient and vorticity isolines for the coupled passive–active control.
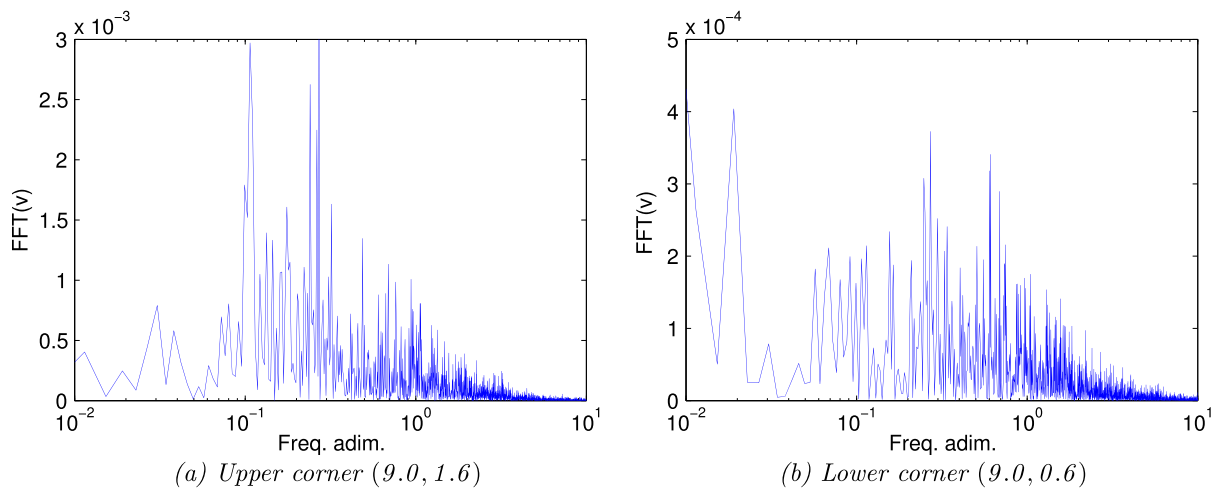

(a) Upper corner (9.0, 1.6)

(b) Lower corner (9.0, 0.6)

Fig. 40. Spectra of the vertical velocity component at points (9.0,1.6) and (9.0,0.6) for the coupled passive–active control.
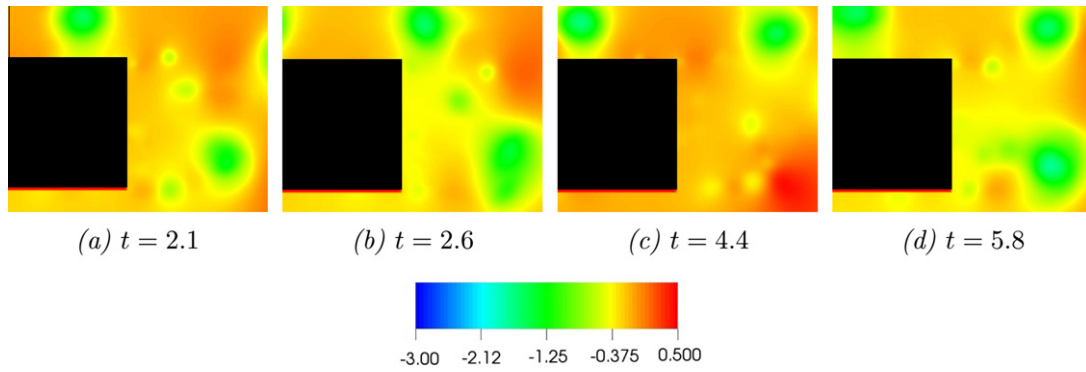
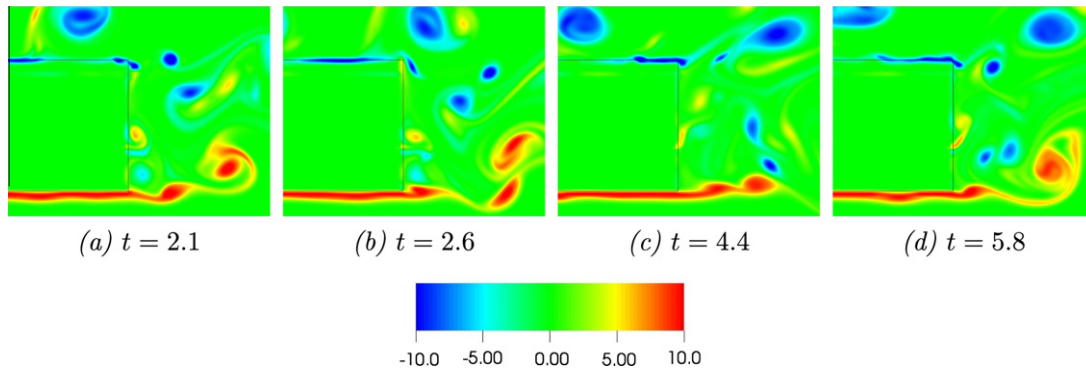**Fig. 42.** Evolution of the pressure field during a shedding cycle for the coupled passive–active control.

Fig. 43. Evolution of the vorticity field during a shedding cycle for the coupled passive–active control.
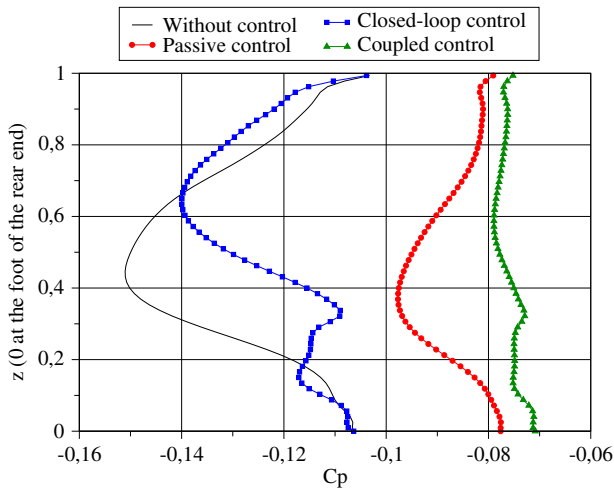

Fig. 44. C_p profile at the rear end of the body for the uncontrolled case, the passive control (case 1), the closed-loop active control at the down point and the coupled passive–active control.

results show clearly the improvement achieved by the coupling as the profile is almost flat and very high.

7. Conclusions

In this paper, several techniques to control the flow around the square back Ahmed body on top of a road are tested, analyzed and carefully compared to the uncontrolled case. The results concerning the active control with blowing jets are mitigated. The steady jet is quite expensive as it is necessary to reach a minimum velocity to obtain a significant change. The pulsed jet is difficult to handle as it is very difficult to synchronize the action and the flow. The closed-loop jet is more relevant as it synchronizes itself to the flow but the changes of the position of the actuator and sensors yield very different results.

The porous layers passive control is more robust, easy to handle and efficient. However it can not be used everywhere. To improve its results a possibility is to couple it to a closed-loop control with a good position of the actuator and sensor. The results obtained in this last case are very promising as a 31% reduction of the drag coefficient is reached. This procedure should give similar results in 3D around a square back Ahmed body but not for the Ahmed body with a $\alpha = 25°$ rear window as the flow characteristics are very different, in particular new lateral vortices develop on the rear window.

References

[1] Angot P, Bruneau C-H, Fabrie P. A penalization method to take into account obstacles in incompressible viscous flows. Numer Math 1999;81:497–520.

[2] Ahmed SR, Ramm G, Faltin G. Some salient features of the time – averaged ground vehicle wake, SAE-paper 840300, 1984.

[3] Bruneau C-H, Fabrie P. Effective downstream boundary conditions for incompressible Navier–Stokes equations. Int J Numer Meth Fluids 1994;19:693–705.

[4] Bruneau C-H, Mortazavi I. Passive control of the flow around a square cylinder using porous media. Int J Numer Meth Fluids 2004;46:415–33.

[5] Bruneau C-H, Mortazavi I. Numerical modelling and passive flow control using porous media. Comput Fluids 2008;37(5).

[6] Bruneau C-H, Mortazavi I, Gilliéron P. Passive control around the two-dimensional square back Ahmed body using porous devices. J Fluids Eng 2008;130:1–33.

[7] Bruneau C-H, Saad M. The 2D lid-driven cavity problem revisited. Comput Fluids 2006;35:326–48.

[8] Brunn A, Wassen E, Sperber D, Nitsche W, Thiele F. Active drag control for a generic car model. In: King, editor, Active flow control, notes on numerical fluid mechanics and multidisciplinary design, vol. 95, 2007, p. 247–59.

[9] Caltagirone J-P. Sur l'intéraction fluide–milieu poreux: application au calcul d'efforts exercés sur un obstacle par un fluide visqueux. CRAS 1994;318:571–7.

[10] Carbou G. Brinkmann model and double penalization method for the flow around a porous thin layer. J Math Fluid Mech 2006;8:1–33.

[11] Chantalat F, Bruneau Ch-H, Galusinski C, Iollo A. Level-set, penalization and cartesian meshes: a paradigm for inverse problems and optimal design. J Comp Phys 2009;228(17).

[12] Cooper KR, The effect of front-edge rounding and rear-edge shapping on the aerodynamic drag of bluff vehicles in ground proximity, SAE paper 850288, 1985.

[13] Duell EG, George AR. Experimental study of a ground vehicle body unsteady near wake, SAE Paper 01-0812, 1999.

[14] Fieldler HE, Fernholz HH. On the management and control of turbulent shear flows. Prog Aero Sci 1990;27.

[15] Gilliéron P. Contrôle des écoulements appliquéà l'automobile. Etat de l'art, Meca Ind: Elsevier; 2002.

[16] Gilliéron P. Detailed analysis of the overtaking process. J Mech Eng 2003;53.

[17] Gilliéron P, Chometon F. Modelling of stationary three-dimensional separated air flows around an Ahmed reference model, ESAIM 7, 1999.

[18] Gilliéron P, Chometon F, Laurent J. Analysis of histeresis and phase shifting phenomena in unsteady three-dimensional wakes. Exp Fluids 2003;35.

[19] Gilliéron P, Spohn A. Flow separations generated by a simplified geometry of an automotive vehicle, IUTAM Symp. Unsteady Separated Flows; 2002.

[20] Guilmineau E. Computational study of flow around a simplified car body. J Wind Eng Ind Aerod 2008;96:1207–17.

[21] Ho CM, Huerre P. Perturbed free shear layers. Ann Rev Fluid Mech 1984;16:365–424.

[22] Kenworthy JS, The flow and mixing in double concentric jets, Ph.D. Thesis University of Sheffield; 1971.

[23] Krajnović S, Davidson L. Numerical study of the flow around the bus-shaped body. ASME J Fluids Eng 2003;125.

[24] Lienhart H, Stoots C, Becker S. Flow and turbulence structures in the wake of a simplified car model (Ahmed model), DGLR Fach Symposium Der AG STAB, 2000.

[25] Martins LF, Ghoniem AF. Simulation of the non-reacting flow in a bluff-body burner: effect of the diamater ratio. J Fluids Eng 1993;115:474–84.

[26] Minguez M, Pasquetti R, Serre E. High-order LES of flow over the Ahmed reference body. Phys Fluids 2008:20–9.

[27] Onorato M, Costelli AF, Garonne A. Drag measurement through wake analysis, SAE paper, 1984, p. 569.

[28] Pastoor M, Henning L, Noack BR, King R, Tadmor G. Feedback shear layer control for bluff body drag reduction. J Fluid Mech. 1984;608:161–96.

[29] Roshko A, Koenig K. Interaction effects on the drag of bluff bodies in tandem. In: Sovran G, Morel T, Mason WT, editors. Symposium on aerodynamic drag mechanisms of bluff bodies and road vehicles, Plenum Press; 1978.

[30] Rouméas M, Gilliéron P, Kourta A. Analysis and control of the near-wake flow over a square-back geometry. Comput Fluids 2009;38:60–70.